

**A Review on Photocatalytic Glass Ceramics:  
Fundamentals, Preparation, Performance Enhancement  
and Future Development**

WANG, Jun, WANG, Mitang <<http://orcid.org/0000-0002-0387-5828>>, TIAN, Yingliang and DENG, Wei

Available from Sheffield Hallam University Research Archive (SHURA) at:

<https://shura.shu.ac.uk/30919/>

---

This document is the Published Version [VoR]

**Citation:**

WANG, Jun, WANG, Mitang, TIAN, Yingliang and DENG, Wei (2022). A Review on Photocatalytic Glass Ceramics: Fundamentals, Preparation, Performance Enhancement and Future Development. *Catalysts*, 12 (10): 1235. [Article]

---

**Copyright and re-use policy**

See <http://shura.shu.ac.uk/information.html>

Review

# A Review on Photocatalytic Glass Ceramics: Fundamentals, Preparation, Performance Enhancement and Future Development

Jun Wang<sup>1</sup>, Mitang Wang<sup>1,\*</sup> , Yingliang Tian<sup>2,\*</sup> and Wei Deng<sup>3</sup>

<sup>1</sup> School of Materials and Chemistry, University of Shanghai for Science and Technology, Shanghai 200093, China

<sup>2</sup> College of Materials Science and Engineering, Beijing University of Technology, Beijing 100124, China

<sup>3</sup> Materials and Engineering Research Institute, Faculty of Science, Technology and Arts, Sheffield Hallam University, Sheffield S1 1Wb, UK

\* Correspondence: btwmt@126.com (M.W.); tianyl@bjut.edu.cn (Y.T.)

**Abstract:** Photocatalytic technology is considered as one of the most attractive and promising technologies to directly harvest, convert and store renewable solar energy for generating sustainable and green energy and a broad range of environmental applications. However, the use of a photocatalyst in powder or coating forms restricts its applications due to its disadvantages, such as difficulty in recovery of nano-powder, secondary pollution, low adhesion between photocatalytic coating and substrate material, short service life of photocatalytic film and so on. The investigation and application of photocatalytic glass-ceramics (PGCs) in water purification, bacterial disinfection, self-cleaning and hydrogen evolution have received extensive attention due to their inherent advantages of low cost, easy fabrication, transparency, chemical and mechanical stability. Real-time solutions to energy shortage and environmental pollution faced by the development of human society can be provided by rationally designing the chemical composition and preparation methods of glass ceramics (GCs). This review introduces the concept and crystallization mechanism of PGCs and expounds on the basic mechanism of photocatalysis. Then, the key point difficulties of GCs' design are discussed, mainly including the methods of obtaining transparency and controlling crystallization technologies. Different modification strategies to achieve better photocatalytic activity are highlighted. Finally, we look forward to further in-depth exploration and research on more efficient PGCs suitable for various applications.

**Keywords:** glass ceramics; photocatalysis; transparency; crystallization; performance enhancement



**Citation:** Wang, J.; Wang, M.; Tian, Y.; Deng, W. A Review on Photocatalytic Glass Ceramics: Fundamentals, Preparation, Performance Enhancement and Future Development. *Catalysts* **2022**, *12*, 1235. <https://doi.org/10.3390/catal12101235>

Academic Editor: Pedro B. Tavares

Received: 17 August 2022

Accepted: 11 October 2022

Published: 14 October 2022

**Publisher's Note:** MDPI stays neutral with regard to jurisdictional claims in published maps and institutional affiliations.



**Copyright:** © 2022 by the authors. Licensee MDPI, Basel, Switzerland. This article is an open access article distributed under the terms and conditions of the Creative Commons Attribution (CC BY) license (<https://creativecommons.org/licenses/by/4.0/>).

## 1. Introduction

Energy shortage and environmental pollution are the two major problems that have faced the development of human society since the 21st century. Therefore, the search for clean and renewable energy and the development of efficient energy storage and conversion technologies are imperative. Photocatalytic technology can directly capture, convert and store renewable solar energy, resulting in sustainable green energy and a wide range of environmental applications. This opens up more tangible possibilities for the development of sustainable energy and technologies [1–3].

Since the discovery of TiO<sub>2</sub> as a photocatalyst by Fujishima and Honda [4] in 1972, a lot of exploration into its photocatalytic properties has been carried out [5–9]. In addition to TiO<sub>2</sub>, the photocatalytic activity of bismuth- and zinc-based compounds also has been preliminarily investigated [10–13]. Most of the research have been conducted by taking raw materials in powder form. Furthermore, TiO<sub>2</sub> coated photoactive self-cleaning Pilkington Activ™ glass has been used for photocatalytic degradation of common pharmaceutical

residues in the aquatic system [14,15]. However, some drawbacks of powdered photocatalysts limit its applications, such as difficulty in recovery of nano-powder, secondary pollution, low adhesion between photocatalytic coating and substrate material, short service life of photocatalytic film and so on. On the other side, glass and glass ceramics (GCs) have been widely used due to their low cost, easy fabrication, high transparency, chemical and mechanical stability, etc. GCs are formed from glasses through the controlled nucleation and crystallization of glasses [16]. PGCs should precipitate crystals with corresponding photocatalytic activity in GCs for various applications. However, there are still considerable research gaps in the application of bulk PGCs in the environmental fields, such as water pollutant degradation, air purification, antibacterial, surface self-cleaning, photocatalytic reduction in CO<sub>2</sub>, photocatalytic hydrogen evolution, etc. [17,18].

The investigation of traditional GCs and functional transparent glass ceramics (TGCs) has been reviewed in previous papers and books [19–25]. However, in recent years, numerous researchers have made new explorations and discoveries in GC systems, manufacturing processes and applications. In the past 20 years, the total number of papers in the field of photocatalytic glass ceramics (PGCs) has increased, and research is, generally, developing further and receiving more attention (Figure 1a). In the past decade, the application of PGCs in the environmental field has mainly focused on surface self-cleaning, antibacterial, water pollution degradation and air purification, but the application of hydrogen evolution and carbon dioxide reduction remains to be studied (Figure 1b). At present, there is little review on the performance improvement and rational design of PGCs. At the same time, few researchers have analyzed the conflicting properties of transparency and crystallinity in detail to discuss the balance between them, let alone systematically summarize and generalize the preparation and modification methods to improve the photocatalytic performance of PGCs. Therefore, this review is compiled to discuss the recent advances in GCs, focusing on the preparation and performance improvements of GCs as photocatalytic materials. Firstly, we introduce the classification of PGCs, including its advantages and applications, with a summarization of the photocatalytic mechanism. Furthermore, the key points of PGCs design were reviewed, including the control of transparency and crystallization for GCs and techniques to achieve better photocatalytic performance. At the end of this paper, a brief generalization of the review was summarized so as to forecast the future research direction of PGCs.

(a)

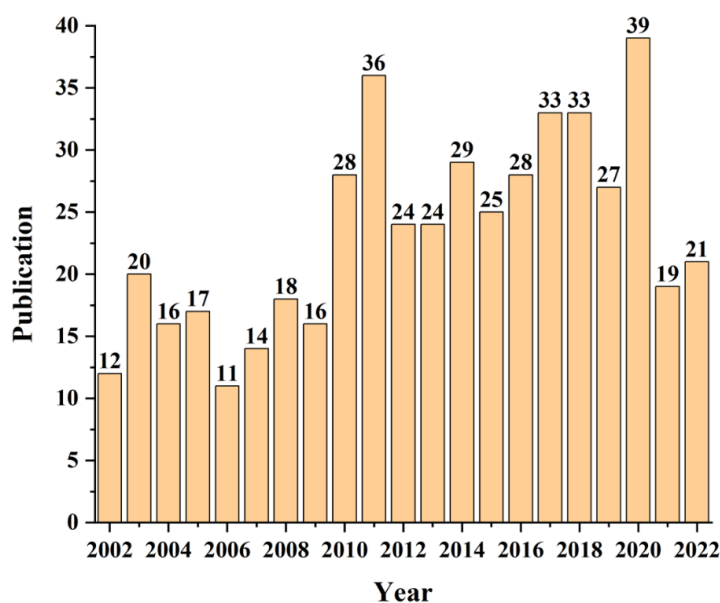
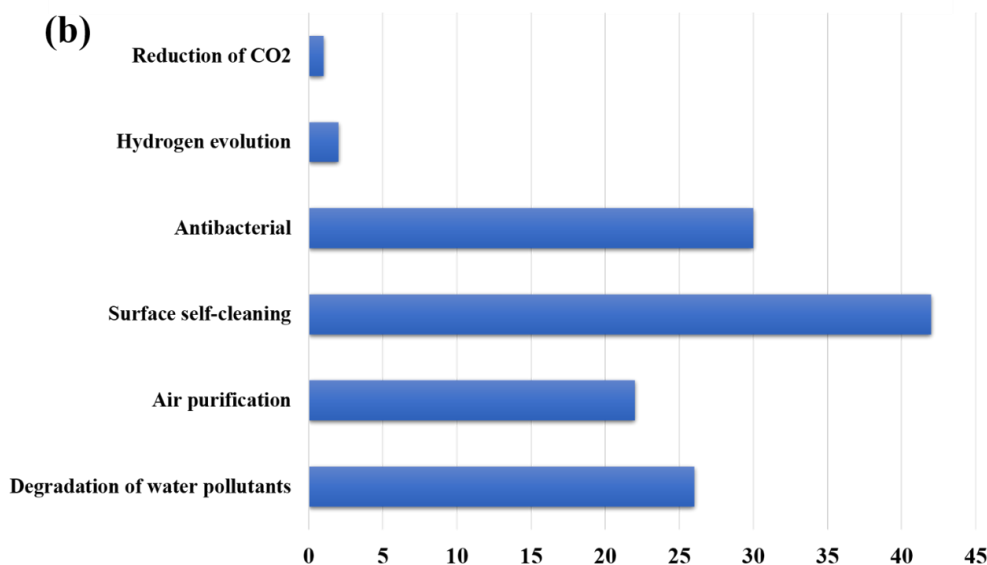


Figure 1. Cont.



**Figure 1.** (a) Annual publications on PGCs (January 2002–September 2022, Web of Science). (b) Publications on various applications of PGCs in the past decade (January 2002–September 2022, Web of Science).

## 2. Photocatalytic Glass-Ceramics (PGCs)

Since the first proposal of GCs by Stookey [26] in the 1950s, numerous researchers have investigated the crystallization of glasses, and many functional GCs have been developed commercially so far [27,28]. GCs are composite multiphase materials with crystallites dispersed in super-cooled liquid and glassy matrices [29]. The parent glasses can be fabricated by melt-quenching techniques above the liquidus temperature. Then, the crystals are nucleated and grow to form GCs, typically with heat treatment. The crystallites formed in the glass not only improve the original properties of the parent glass, but also may provide completely new properties to the parent glass [30]. The composition, microstructure and phase assemblage determine the properties of GCs [31]. Different microstructures can be obtained by adjusting the composition and heat treatment process. Furthermore, another significant advantage of GCs is their transparency. To obtain a TGC, it is necessary to minimize the light attenuation caused by scattering and absorption. In fact, in order to ensure the transparency of the GCs, the nanocrystals are made sufficiently small (<30 nm) by controlling the crystallization process. On the other hand, when large crystals, up to micrometer scale, are present in TGCs, the refractive index difference between the crystalline and the glassy phase must be very small (<0.01) to avoid loss of transparency. The properties of GCs combine the important features of glass and polycrystalline ceramics and have many potential applications, such as optical, dental, machining, thermal, construction, bioactive and electrical applications, etc.

### 2.1. Mechanism of Photocatalysis

In 1967, photocatalysis was discovered by Fujishima Akira and Kenichi Honda, also known as the “Honda–Fujishima Effect”, which is a pioneering study of photocatalysis. In 1972, Fujishima and Honda [4] first reported a photochemical system consisting of a TiO<sub>2</sub> photoelectrode and platinum electrode, capable of splitting water into hydrogen and oxygen, thus opening up the new field of semiconductor photocatalysis. The photocatalysis process has potential applications in the evolution of hydrogen, reduction of carbon dioxide (CO<sub>2</sub>), wastewater treatment, air-cleaning, surface self-cleaning, detoxification and bacterial disinfection [32,33].

Thus far, the fundamental mechanism of photocatalysis has been well proposed, as shown in Figure 2. Basically speaking, the heterogenous photocatalysis process is initiated with the absorption of light (or radiation) having energy equal to or greater than the band

gap energy ( $E_g$ ) of targeted semiconductor material [34].  $E_g$  is defined as the difference between the filled valence band (VB) and the empty conduction band (CB). When photons with energy equal to or higher than  $E_g$  reach the surface of the photocatalyst, they will cause molecular excitation. Some electrons are excited from VB to CB of the semiconductor and create holes in the valence band. After the initiation of these photogenerated electron ( $e^-$ )-hole ( $h^+$ ) pairs, these can either recombine and dissipate the absorbed energy in the form of heat or can migrate to the surface for catalytic redox reactions [35]. During catalytic redox reactions, these holes ( $h^+$ ), being good oxidizing agents, oxidize adsorbed water ( $H_2O$ ) to form hydroxyl radicals ( $\cdot OH$ ). This  $\cdot OH$  will then lead to the production of strong oxidizing  $HO^\bullet$  radicals. Meanwhile, the negative electrons being strong reducing agents reduce adsorbed oxygen ( $O_2$ ) to form a superoxide anion ( $O_2^{\bullet -}$ ). This superoxide anion also produces  $HO^\bullet$  radicals via the formation of  $HO_2^\bullet$  radicals and  $H_2O_2$  [35]. These reactive oxidizing species (ROS) react with adsorbed pollutants such as organic compounds and decompose them, thereby degrading them into  $CO_2$ , water and, sometimes, other less harmful species [36].

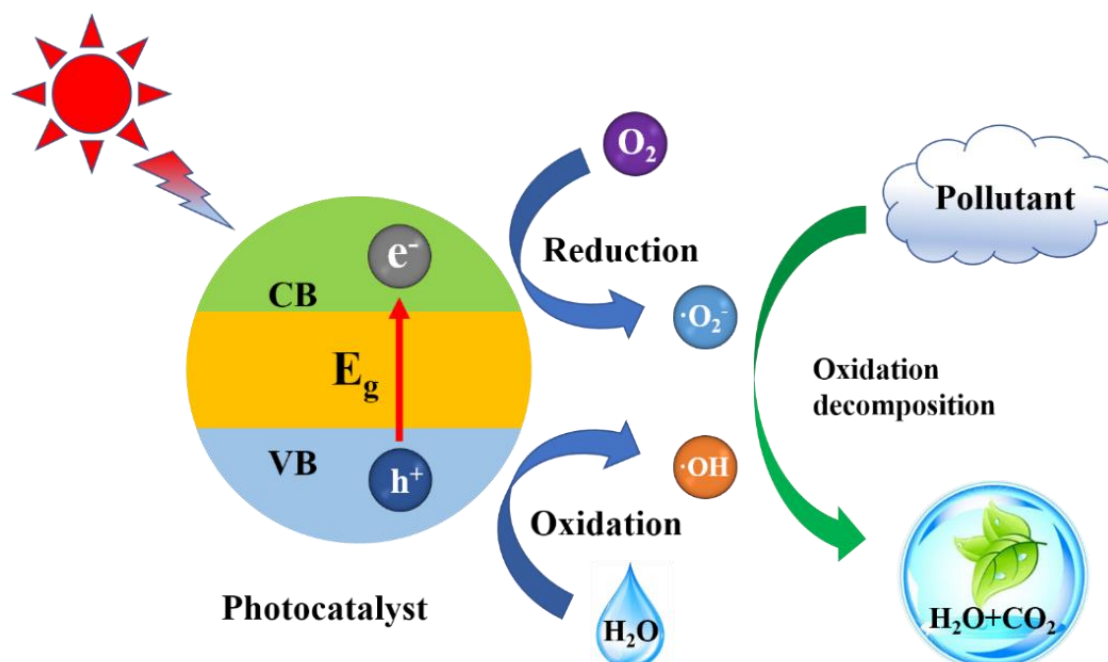


**Figure 2.** The schematic mechanism of heterogeneous photocatalysis.

The electron–hole recombination step is undesirable as it will result in low photocatalytic efficiency and waste the energy supplied by the photon. Therefore, reducing the charge recombination rate in the body and on the surface of the semiconductor is one of the most effective methods to improve the photocatalytic activity. For the surface charge utilization, the large onset overpotential and sluggish kinetics are two key factors limiting the surface photocatalytic efficiency of reduction and oxidation reactions. Usually, shortening the diffusion length of photo-generated charge carriers or constructing interfacial electric fields could efficiently reduce the recombination rates, thus substantially enhancing the photocatalytic activity [37]. Moreover, to design highly efficient photocatalysts suitable for various photocatalytic applications, light harvesting efficiency ( $\eta_{\text{abs}}$ ), charge separation efficiency ( $\eta_{\text{cs}}$ ), charge migration and transport efficiency ( $\eta_{\text{cmt}}$ ) and charge utilization efficiency ( $\eta_{\text{cu}}$ ) should be comprehensively considered and optimized [38]. Despite the significant advances in heterogeneous photocatalysis, there are still many challenges related to the further enhancements of light harvesting (especially for the visible light region) and reduction in the recombination rates of photo-induced electrons and holes, separation and utilization.

## 2.2. Classification of PGCs

Photocatalytic GCs can provide corresponding photocatalytic activity due to the crystals precipitated during the heat treatment. There are two distinct crystallization mechanisms involved in the preparation of GCs, i.e., surface and volume (bulk) crystallization. Research has shown that the devitrification of glass with  $Trg < 0.58$  ( $Trg = Tg/Tm$ , where  $Tm$  is melting temperature) is dominated by volume crystallization, and surface crystallization may also occur [39,40]. Homogeneous nucleation is more favorable in this case because the maximum nucleation temperature is lower than  $Tg$ . If  $Trg > 0.6$ , the nucleation rate near  $Tg$  is low and the heterogeneous nucleation becomes dominant, which is often observed in the surface crystallized GCs. It has been found that GCs with a small density difference ( $<10\%$ ) between the crystalline and glassy phases typically undergo homogeneous nucleation and, thus, appear to be dominated by volume nucleation [41]. However, if the density difference is large, the high elastic deformation energy ( $\Delta G_E$ ) at the interface may inhibit bulk crystallization, and GC is more inclined to surface crystallization [42].

Either surface crystallization, bulk crystallization or a combination of the two can be used to design GCs with desired properties. Different from other photocatalytic materials, photocatalytic active GCs have the advantages of being easy to produce and process into different shapes (sheets, plates, fibers and rods) and sizes and having excellent chemical stability, leading to broader applications in photocatalysis. As shown in Figure 3, photocatalytic active GCs have various applications in the environmental fields, such as degradation of water pollutants, air purification, surface self-cleaning, antibacterial, photocatalytic hydrogen evolution and photocatalytic reduction in  $CO_2$ , etc.

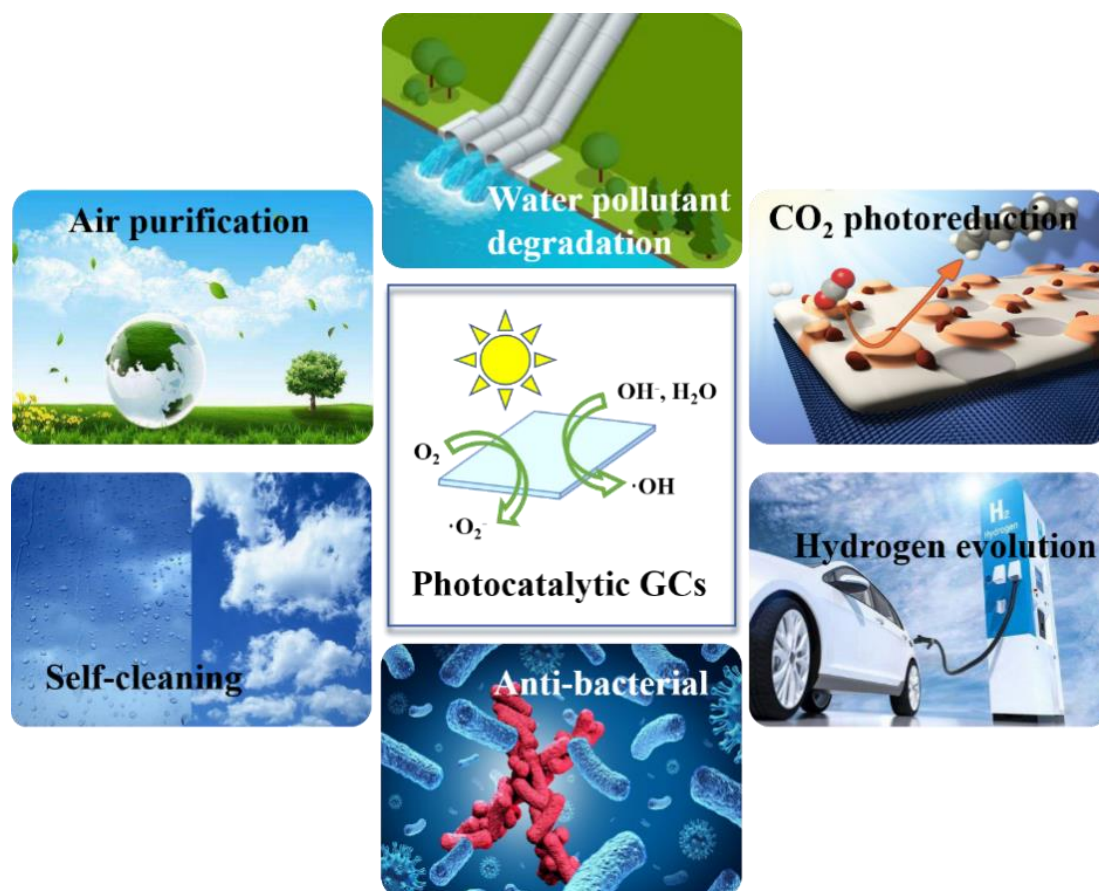
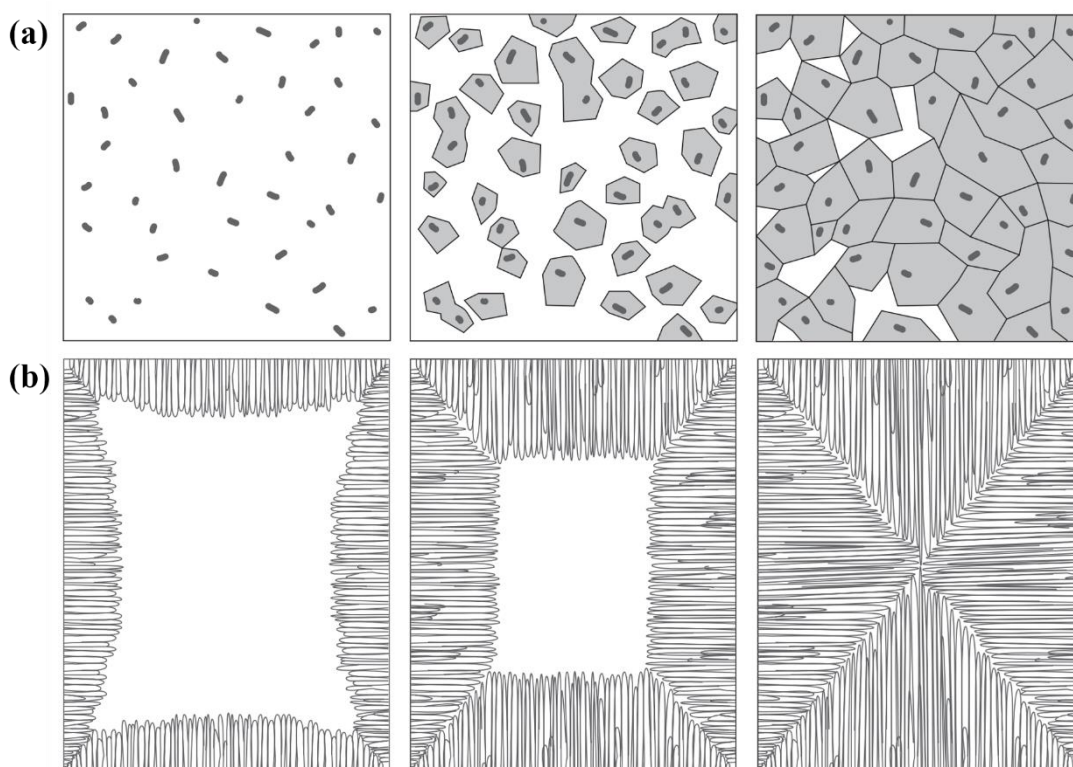


Figure 3. Potential environmental applications of PGCs.

### 2.2.1. Volume Crystallization

In volume crystallized PGCs, the photocatalytic active crystallites are dispersed on the surface as well as in the bulk of GCs. Indeed, volume crystallization is often required to obtain a wide range of novel TGC materials with good optical homogeneity. In this case, nuclei in glass continue to grow linearly with volume until they are hindered by adjacent crystals. This is followed by secondary growth, which causes smaller crystals to fuse in favor of larger crystals (see Figure 4a).



**Figure 4.** (a) Bulk crystallization. (b) Surface crystallization. Reprinted with permission from Ref. [22].

It is well known that  $\text{TiO}_2$  has excellent photocatalytic activity. Therefore, an attempt can be made to form  $\text{TiO}_2$  crystals in glass to obtain PGCs. Yazawa et al. [43] have successfully prepared rutile-type  $\text{TiO}_2$  GCs from the  $\text{SiO}_2\text{-Al}_2\text{O}_3\text{-B}_2\text{O}_3\text{-CaO-TiO}_2$  glass system. The photocatalytic activity of this GC was about four times larger than that of a  $\text{TiO}_2$  coated photocatalyst fabricated by the sol-gel process. In this direction, Singh et al. [44] have fabricated the stable rutile phase of  $\text{TiO}_2$  nanocrystals in the  $5\text{CaO-65B}_2\text{O}_3\text{-10BaO-Al}_2\text{O}_3\text{-20TiO}_2\text{-10ZnO}$  (mol%) glass by a heat treatment process and investigated the effect of different heat treatments on the transparency and photocatalytic activity of GCs. The parent glass sample was referred to as the CBBATZ sample. The parent glass was heat treated with three different crystallization times (3, 5 and 10 h at  $630^\circ\text{C}$ ) and the resulting GCs were designated CBBATZ-1, CBBATZ-2 and CBBATZ-3, respectively. All heat-treated samples were transparent in the wavelength range of 800–405 nm. Hence, we can easily see that, even with the formation of  $\text{TiO}_2$  crystals in glass samples, the samples were still transparent in the visible region. It means that the most important property of glass (transparency) is still preserved in glass nanocomposite. Figure 5 shows the photocatalytic activity of the photocatalytic ink test and MB dye degradation test. With the increase in heat treatment time, the photocatalytic activity increased. Compared to CBBATZ, CBBATZ-1 and CBBATZ-2 samples, GC CBBATZ-3 showed the best degradation performance of Resazurin ink and MB dye. From CBBATZ-1 to CBBATZ-3, the bandgap of the samples decreased and the  $\text{TiO}_2$  crystallinity increased, so the photocatalytic activity of CBBATZ-3 was more impressive. GCs containing anatase-type  $\text{TiO}_2$  crystals or  $(\text{TiO})_2\text{P}_2\text{O}_7$  crystals were obtained by Jie

Fu [45] through thermal treatment of binary  $\text{TiO}_2\text{-P}_2\text{O}_5$  glasses with 69 mol% and 76 mol%  $\text{TiO}_2$ . Consistent with the above, the activity of photocatalytic degradation of methylene blue (MB) was enhanced with the increase in anatase  $\text{TiO}_2$  crystalline phases. In the other report of Jie Fu [46], a GC containing Nasicon-type crystal  $\text{MgTi}_4(\text{PO}_4)_6$  was prepared by heat-treating  $\text{MgO-TiO}_2\text{-P}_2\text{O}_5\text{-SiO}_2$  glasses, which exhibited a strong ability to decompose methylene blue (MB) and acetaldehyde and super-hydrophilicity under UV irradiation.

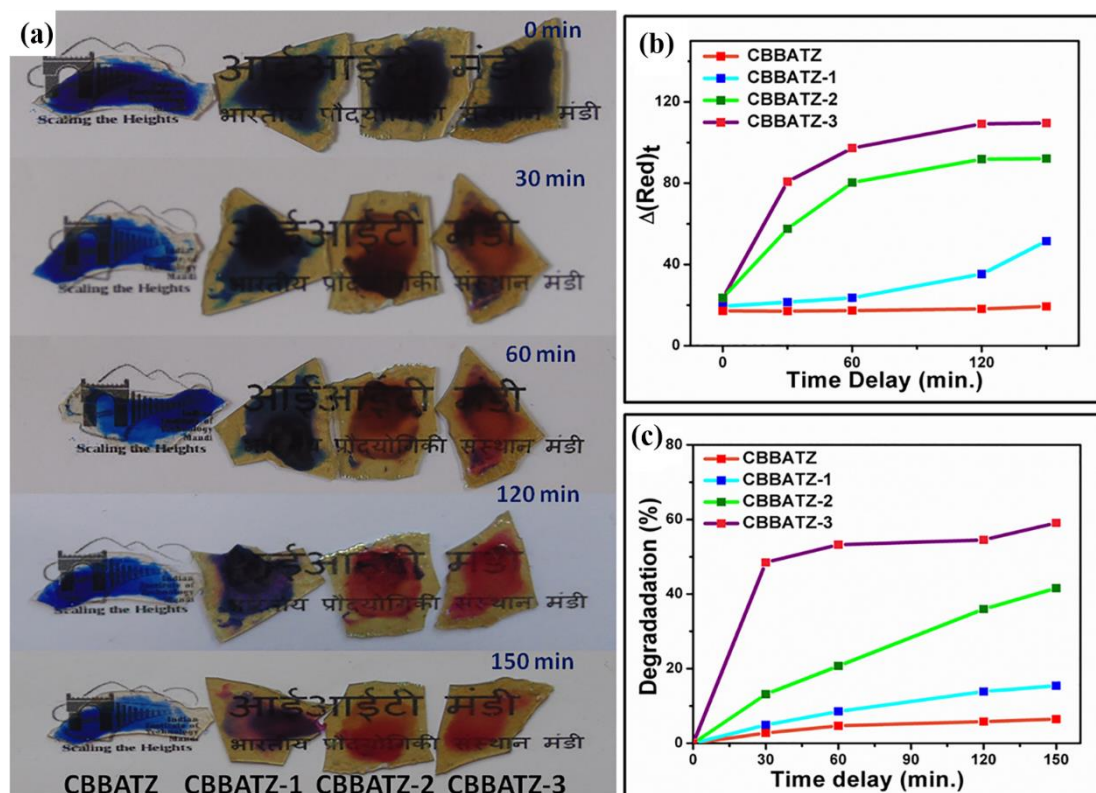


**Figure 5.** (a) Digital photographs of CBBATZ, CBBATZ-1, CBBATZ-2 and CBBATZ-3 samples at time  $t = 0, 30, 60, 120$  and  $150$  min during an ink test. (b)  $C_t/C_0$  vs. time plot for all samples. (c) Percentage degradation in absorbance of MB dye with time for all samples. Reprinted with permission from Ref. [44].

Like  $\text{TiO}_2$ , many other photocatalytic crystallites can also be used to form photocatalytic activity GCs. Margha et al. [47] have prepared a transparent photoactive GC material containing a high content of a ZnO component (up to 40%) for the glass composition  $\text{SiO}_2, \text{ZnO}, \text{B}_2\text{O}_3, \text{Na}_2\text{O}, \text{K}_2\text{O}, \text{P}_2\text{O}_5, \text{Li}_2\text{O}$  and  $\text{BaO}$ . This GC showed proper photocatalytic activity for the degradation of Red SPD Cotton dye as a model compound. Maximum removal (76%) was achieved in the case of the sample containing 30 wt% of ZnO and heat treated at  $450^\circ\text{C}$  for 10 h. Singh et al. [48] also fabricated transparent ZnO crystallized GCs from the  $9.35\text{K}_2\text{O-9.35CaO-42.05ZnO-23.36B}_2\text{O}_3\text{-9.35SiO}_2\text{-6.54Al}_2\text{O}_3$  (in mol%) glass system. The results showed that the degradation ability of the photocatalytic Rhodamine B (RB) dye is enhanced with increasing crystallization time from 30 to 90 min at  $700^\circ\text{C}$  due to the reduced band gap (3.75 to 3.14 eV) of GC samples heat-treated for 30 to 90 min. As shown in Figure 6, they also evaluated the antibacterial properties of the samples by *Escherichia coli* (Gram-negative bacteria). It is evident that ZnO crystallized glass powders (ZnO-1, ZnO-2 and ZnO-3) have significant anti-*E. coli* activity, and the antibacterial properties increase with the increase in the crystallization in the glass matrix. Interestingly, it was found that the ZnO-3 glass could completely eradicate bacteria under UV irradiation for 60 min, which indicated its promising antibacterial properties.

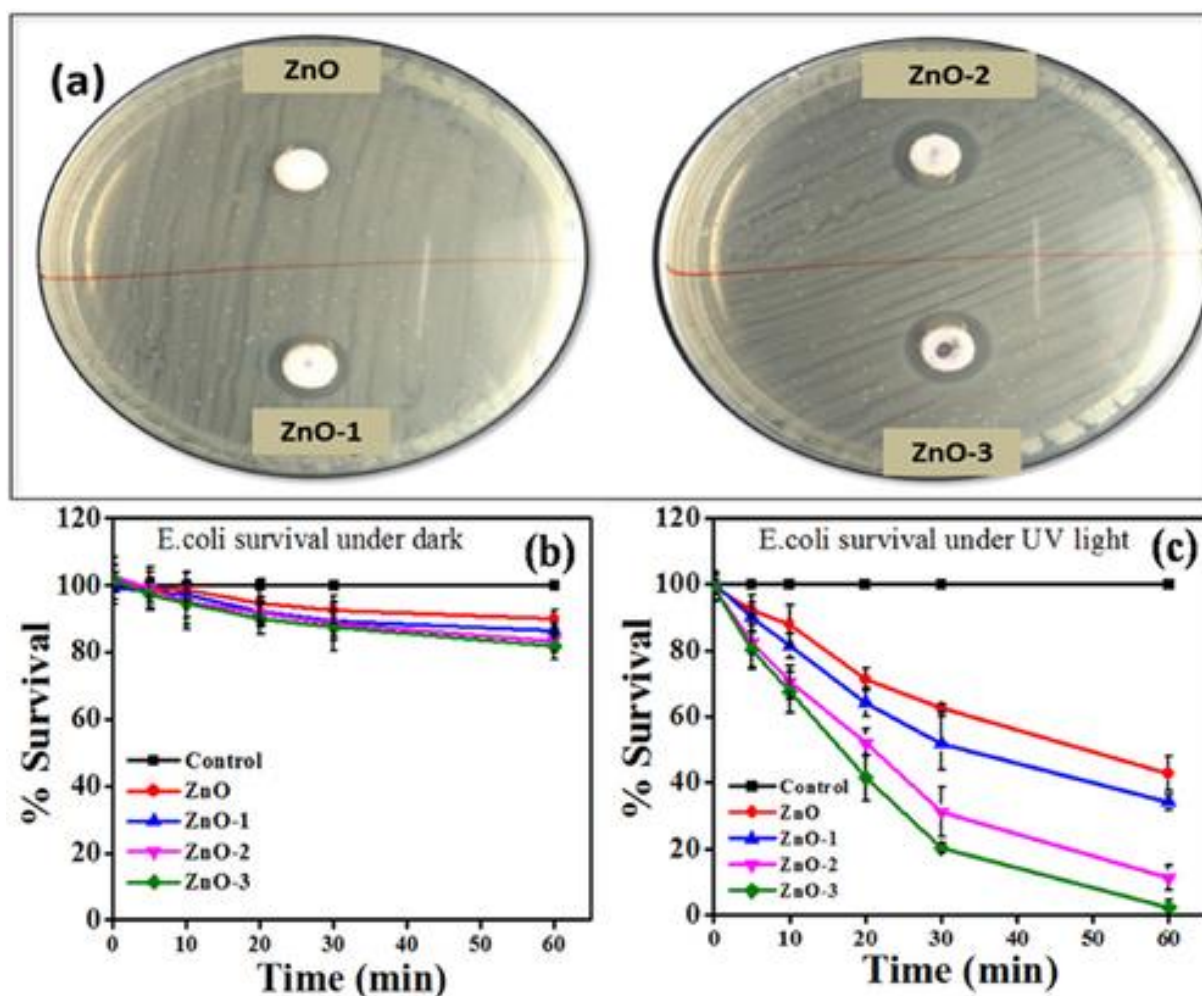


**Figure 6.** Antibacterial activity of ZnO glasses. (a) Disk diffusion test. Survival (in %) of *E. coli* after treatment with ZnO glasses (plate form) (b) under dark and (c) under UV irradiation (360 nm). Reprinted with permission from Ref. [48].

### 2.2.2. Surface Crystallization

When bulk crystallization is activated, surface crystallization will dominate. Surface crystallization generally relies on surface nucleation initiated through tribochemical activation or other methods. Then, surface crystallization proceeds vertically to the interior of the glass, and the crystal usually exhibits a strong preferential growth orientation (see Figure 4b). Surface crystallization is more meaningful for GCs to obtain efficient photocatalytic activity. However, in general, the preferred growth direction of crystal diffusion is into the glass points to the glass interior. Thus far, although many studies have prepared surface-crystallized GCs, their photocatalytic activity has not been explored. Almeida et al. [49] prepared niobate glasses and ceramics  $((x\text{Nb}_2\text{O}_5 (0.5-x)\text{P}_2\text{O}_5) 0.5\text{Li}_2\text{O})$  by the melt-quenching method and detected  $\text{LiNbO}_3$  crystals in samples with high niobium concentration. Differently, Murugan et al. [50] fabricated transparent glasses in the system  $(100-x)\text{Li}_2\text{B}_4\text{O}_7-x\text{SrBi}_2\text{Ta}_2\text{O}_9$  ( $0 < x < 20$ ) via a splat-quenching technique. The XRD of the glass-ceramic composites for  $10 < x \leq 20$  depicts only the presence of monophasic crystalline  $\text{SrBi}_2\text{Ta}_2\text{O}_9$  (SBT). On the other hand, the GC composites for  $x \leq 10$  show the presence of  $\text{Li}_2\text{B}_4\text{O}_7$  (LBO) crystalline peaks in addition to those of SBT. It implies that higher (>10 mol%) concentrations of SBT prevent the crystallization of LBO glass. Further, it is confirmed that the LBO crystallization is confined only to the surface of the sample, while that of SBT was found to be a bulk crystallization process. Plate-like non-porous glass can achieve photocatalysis by crystallizing only at the surface. Laser induced crystallization

is one of the most common techniques for growing the desired photocatalytic active crystals on the surface of GCs [29,51]. In addition, there are unconventional methods to engage bulk photocatalytic active crystals, such as using porous/etched/leached GCs and using a powdered form of GC.

Bulk crystallization is more beneficial in obtaining GCs with high transparency, while surface crystallization is of great significance to the photocatalytic effect of PGCs. In addition, if the transparency is high enough, the photocatalytic crystals on the inner surface of GCs can be maximally activated during the photocatalytic process, resulting in efficient photocatalytic performance. A detailed introduction to the transparency and controlled crystallization of GCs is presented in Section 3.

### 3. Design and Fabrication of Photocatalytic Glass Ceramics (PGCs)

Compared with other photocatalytic materials, PGCs have various advantages. However, due to the inherent drawbacks of GC materials, rational design must be carefully considered to obtain the best photocatalytic performance. Figure 7 summarizes the design considerations for the detailed composition, structure and performance of the GC photocatalysts.

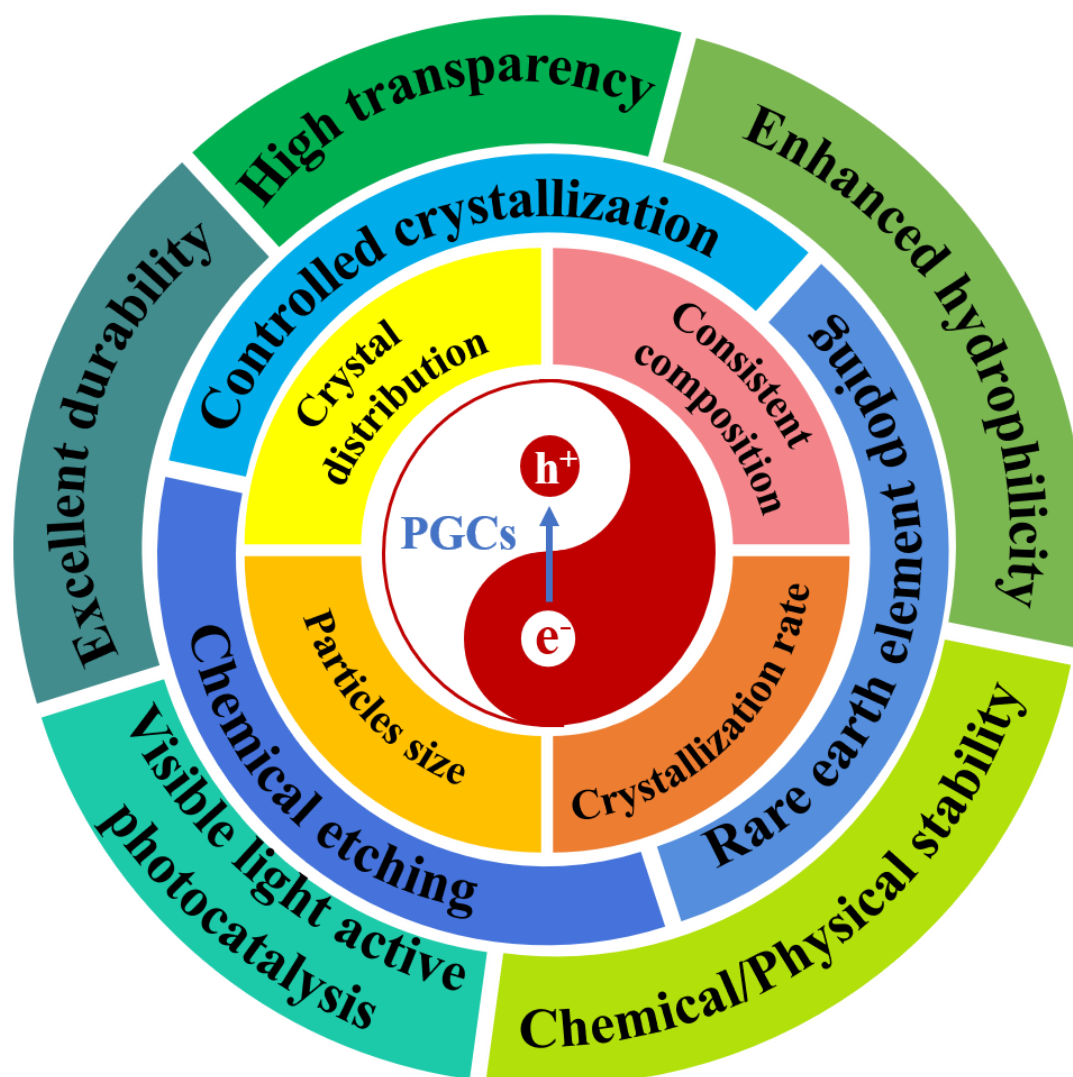


Figure 7. Schematic representation of design considerations of PGCs.

### 3.1. Transparency

Transparency is one of the most important properties of GCs. TGCs are most wanted in the photocatalytic oxidation process to reduce the turbidity in the photoreactor and to activate more photocatalyst particles. However, the formation of crystals within the glass matrix reduces transparency and becomes translucent, sometimes even opaque. The reduction in transparency is mainly due to high optical scattering, and more ionic/atomic absorption occur [28], as described by:

$$I_T = I_0 \cdot \exp[-(\alpha + \sigma) \cdot l] \quad (1)$$

where  $I_T$  and  $I_0$  are the intensity of the transmitted and the incident light, respectively,  $\alpha$  and  $\sigma$  are the absorption coefficient and the turbidity of the sample, respectively, and  $l$  is the sample thickness. Therefore, in order to maintain the high transparency of the glass, the scattering loss (i.e., turbidity) must be minimized.

For GCs containing crystals with sizes much smaller than the wavelength of light, the crystals are widely separated (for diluted systems). The Rayleigh–Gans scattering model gives the turbidity as [52]:

$$\sigma_P \approx \frac{2}{3} NVk^4 R^3 (n\Delta n)^2 \quad (2)$$

where  $N$  is the number density of the crystallites,  $R$  and  $V$  are the radius and volume of the crystal phase, respectively,  $n$  is the refraction index of the crystal and  $\Delta n$  is the refractive index difference between the glassy and the crystal phase, and  $k = 2\pi/\lambda$ , where  $\lambda$  is the wavelength of light.

From the equation above, it is clear that the turbidity is inversely proportional to  $\lambda^4$ , which is known as Rayleigh scattering. In addition, the turbidity is extremely sensitive to the size of the particles ( $\propto R^3$ ) as well as the difference in the refractive index of the ( $\propto \Delta n^2$ ). Practically, highly transparent TGCs (in the visible range) without a noticeable scattering effect can be obtained for crystal radius  $R < 15$  nm and refractive index difference  $\Delta n < 0.1$ . This condition does not have to be stringently obeyed for a sufficiently small  $\Delta n$  ( $\sim 0.01$ ).

It is known that the Rayleigh–Gans model overestimates the light attenuation due to scattering for concentrated particle dispersions. A quasi-continuum model has been developed by Andreev [53] and Hopper [54] for the description of interfering individual particles that produce a large compensation effect. In this model, in addition to requiring the particle size to be much smaller than the wavelength of light, the distance between particles should not be less than the particle radius, but, rather, at least six times the particle radius. The turbidity under such condition is given by:

$$\sigma_c \approx \left[ \left( \frac{2}{3} \times 10^{-3} \right) k^4 \theta^3 \right] (n\Delta n)^2 \quad (3)$$

where  $\theta = a + W/2$  is the mean phase width ( $W$ : the inter-particle distance). According to this model, high transparency can be still achieved for particle size  $< 30$  nm and refractive index difference ( $\Delta n$ ) up to 0.3.

In summary, it is clear that two possibilities exist for producing a transparent crystal-glass system. In one case, nucleation and crystal growth rates should be controlled to precipitate nanocrystals (NCs) and avoid overgrowth and coarsening. The dispersed crystalline phases are sufficiently small in size that they produce no effective scattering, even at the shorter wavelengths of the visible spectrum. In the other case, the refractive index difference between all crystalline and amorphous phases must be minimized, and the birefringence within any single crystalline phase must be small.

The above statement is limited to the case where the crystallite size is much smaller than the wavelength of incident light. For scattering of particles comparable in size to the wavelength of light, only  $\Delta n \sim 0$  in the GC can maintain high transparency.

Actually, the magnitude of transparency of GCs affected by crystallite size and refractive index difference is mainly determined by chemical composition and the heat treatment

process. Prasad et al. [55] reported the transparent glasses in the composition  $(100 - x)\text{Li}_2\text{B}_4\text{O}_7 - x(\text{SrO} - \text{Bi}_2\text{O}_3 - \text{Nb}_2\text{O}_5)$  (where  $x = 10, 20, 30, 40, 50$  and  $60$ , in molar ratio) and obtained the compositional dependence of the refractive indices at  $570 \text{ nm}$  of the GCs. The result indicated that the refractive index increased notably with the increase in the  $\text{SrBi}_2\text{Nb}_2\text{O}_9$  composition  $x$ . In addition, Molla et al. [56] fabricated  $\text{Bi}_4\text{Ti}_3\text{O}_{12}$  (BiT) crystals in the  $\text{K}_2\text{O} - \text{SiO}_2 - \text{Bi}_2\text{O}_3 - \text{TiO}_2$  (KSBT) system by conducting controlled heat treatments at different temperatures and durations. From the spectra in Figure 8a, it is seen that with increasing BiT content in the glass at  $1150^\circ\text{C}$ , transmission of the glass in the wavelength range of  $300 - 1100 \text{ nm}$  decreases. In addition, the effect of melting temperature on the transmission properties of BiT45 glass was investigated, and the transmission properties in the visible wavelength range decreased significantly with increasing melting temperature (Figure 8b).

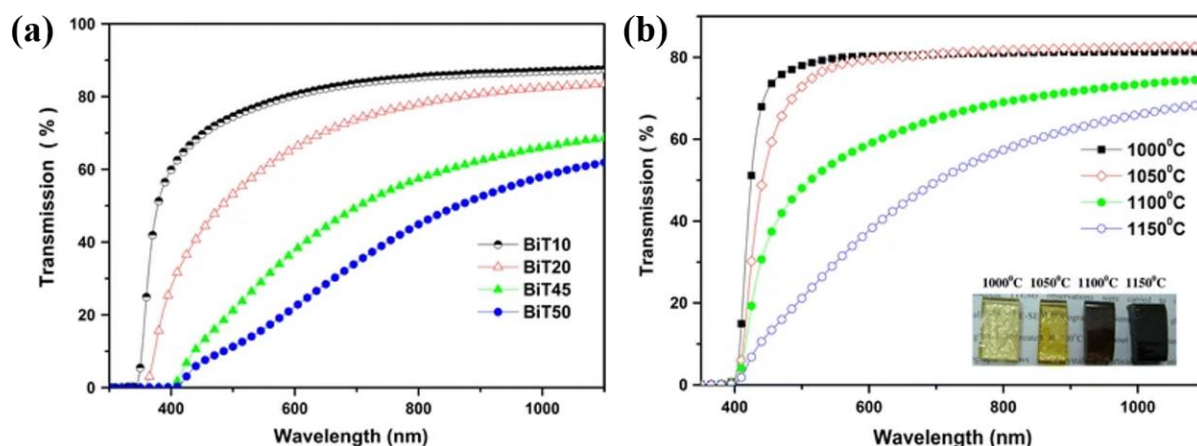


**Figure 8.** Transmission spectra of BiT glasses. (a) Transmission spectra of BiT10, BiT20, BiT45 and BiT50 glasses melted at  $1150^\circ\text{C}$ . (b) Transmission spectra of BiT45 glasses melted at  $1000, 1050, 1100$  and  $1150^\circ\text{C}$ . Inset is the photograph of the glasses showing their visual transparency. Reprinted with permission from Ref. [56].

In addition to chemical composition, the crystal size after heat treatment also has a distinct influence on transparency. Lin et al. [57] presented a simple and universal method for fabricating various kinds of metal or semiconductor nanoparticle (MSNP) glass composites by using metallic Al as a reducing agent in the raw materials of the glass batches. Bi crystals were precipitated in  $10\text{Na}_2\text{O} - 48\text{B}_2\text{O}_3 - 2\text{Al} - 40\text{SiO}_2 - 4\text{Bi}_2\text{O}_3$  glass. The heat treatment temperature and holding time can control the particle size, and the heat treatment can also change the color of the glasses. In general, the larger grain size will bring about the increase in turbidity, and the Mie scattering effect will become prominent for the large refractive index difference between the fabricated nanocrystals and glass matrix [58]. Indeed, the crystal's size must remain smaller than the incident wavelength to avoid too much light scattering in order to maintain the transparency of GC. Masai et al. [59] prepared a single  $\text{TiO}_2$  phase GC in the  $5\text{CaO} - 65\text{B}_2\text{O}_3 - 10\text{Bi}_2\text{O}_3 - \text{Al}_2\text{O}_3 - 20\text{TiO}_2$  glass composition. Although the refractive index difference between the rutile  $\text{TiO}_2$  phase and the glass matrix is relatively large ( $n > 0.8$ ), the obtained GC still has high transparency. This is mainly due to the size of the crystals being much smaller than the wavelength of the incident light.

In the case of polycrystalline precipitation, control of transparency becomes more complicated. The GCs in the  $\text{Bi}_2\text{O}_3 - \text{K}_2\text{O} - \text{TiO}_2 - \text{P}_2\text{O}_5$  system were elaborated by Haily et al. [60]. Different crystalline phases are obtained in the matrix glass as the heat treatment proceeds. The color of the glass samples containing  $\text{Bi}_2\text{O}_3$  is brown as well as the glass free of  $\text{Bi}_2\text{O}_3$  presents blue. The XRD pattern of  $x\text{Bi}_2\text{O}_3 - (20 - x)\text{K}_2\text{O} - 30\text{TiO}_2 - 50\text{P}_2\text{O}_5$  ( $x = 5, 10, 15$ ) GCs implied the appearance of  $\text{KTi}_2(\text{PO}_4)_3$  and  $\text{BiPO}_4$  phase. With a further increase of

$\text{Bi}_2\text{O}_3$  content, there is an increase in the content of the  $\text{BiPO}_4$  phase. The complexity of crystal types determines the opacity of GCs.

For GCs with almost the same composition of the glassy and crystalline phases, the refractive indices can be easily matched. This type of GC can minimize scattering loss and provide high transparency. During the crystallization of such GCs, local structural changes are minimal and ion diffusion paths are the shortest. Examples of such TGCs can be found in chapter 2 in Ref. [61]. Sharma et al. [62] exhibited the formation of  $\text{Bi}_4\text{B}_2\text{O}_9$  crystals embedded in  $2\text{Bi}_2\text{O}_3\text{-B}_2\text{O}_3$  (BBO), the host glass matrix. In BBO GCs, the crystals are uniformly dispersed in the glass matrix in the nano range. The crystal and the matrix glass composition are almost identical so that the transparency of the GC is appreciable. Unfortunately, as the heat treatment time increases, the GC becomes darker. Likewise, Singh et al. [63] precipitated a TGC with  $\text{SrBi}_2\text{B}_2\text{O}_7$  crystals from  $\text{SrO-Bi}_2\text{O}_3\text{-B}_2\text{O}_3$  (SBBO). From the UV-Vis absorption spectra, transmission spectra of the GC showed almost 60–80% transparency in the 500–800 nm spectral range. Despite the presence of  $\text{SrBi}_2\text{B}_2\text{O}_7$  crystals on the surface, GC was still quite transparent, probably due to the close matching of the refractive indices of the crystal and glass phases. However, the transparency of the SBBO GC is gradually lost, accompanied by asymmetric, tightly packed variable grains on the surface, increasing in size from 10  $\mu\text{m}$  to 50  $\mu\text{m}$ .

It should be noted that the same chemical composition of both the glass matrix and crystal does not guarantee the transparency in the GC, and the matching degree of their refractive indices and interface microstructure between the glassy matrix and precipitated crystallites must also be considered. Bertrand et al. [64] achieved a new GC in the  $\text{Bi}_2\text{O}_3\text{-Nb}_2\text{O}_5\text{-TeO}_2$  ( $\text{Bi}_{0.5}\text{Nb}_{0.5}\text{Te}_3\text{O}_8$ ) system. Although the glassy matrix and the crystals have an identical chemical composition, GCs tend to become opaque with crystal nucleation, and growth occurs gradually. As the crystallization process progresses, the optical transmittance of GCs decreases due to the mismatch of refractive indices as well as some micro cracks that appear at the glassy matrix/crystalline droplet interface at some point.

### 3.2. Controlled Crystallization

The fabrication of GCs can be viewed as the synthesis of crystals through solid-state confined reactions in supercooled glass. The crystals formed in the glassy matrix are the product of the reaction between the glass components, yet in the solid state. This solid-state reaction can be triggered by increasing the temperature (i.e., thermal treatment), which is the most popular technique for GC fabrication. Glass can be made by fusion quenching techniques above liquid temperatures. A schematic diagram of glass' transition to GC is shown in Figure 9. In most instances, the cooling rates should be greater than the critical rate to obtain glass ( $q > q_c$ ), where  $q_c = \frac{T_L - T_N}{\delta_t}$ , with  $T_N$  being nose temperature and  $t$  being time.  $T_N$  represents the temperature at which the crystal fraction of  $10^{-6}$  is achieved in the shortest time ( $\delta_t$ ). GCs are usually obtained from parent glass by heat-treating for crystal nucleation and growth. Some GCs are formed directly during cooling from melt using cooling rate  $q \leq q_c$ .  $2\text{Bi}_2\text{O}_3\text{-B}_2\text{O}_3$  (BBO), TGC is obtained by melt-quenching and heat treatment [62]. The XRD of an as-quenched sample illustrates the presence of nanocrystals, which indicates that a small amount of crystals is precipitated during the cooling of the melt. Moreover, with heat treatment of the as-quenched glass at 380 °C for 1, 2 and 3 h to control the crystallization process, the samples all precipitated  $\text{Bi}_4\text{B}_2\text{O}_9$  crystals.

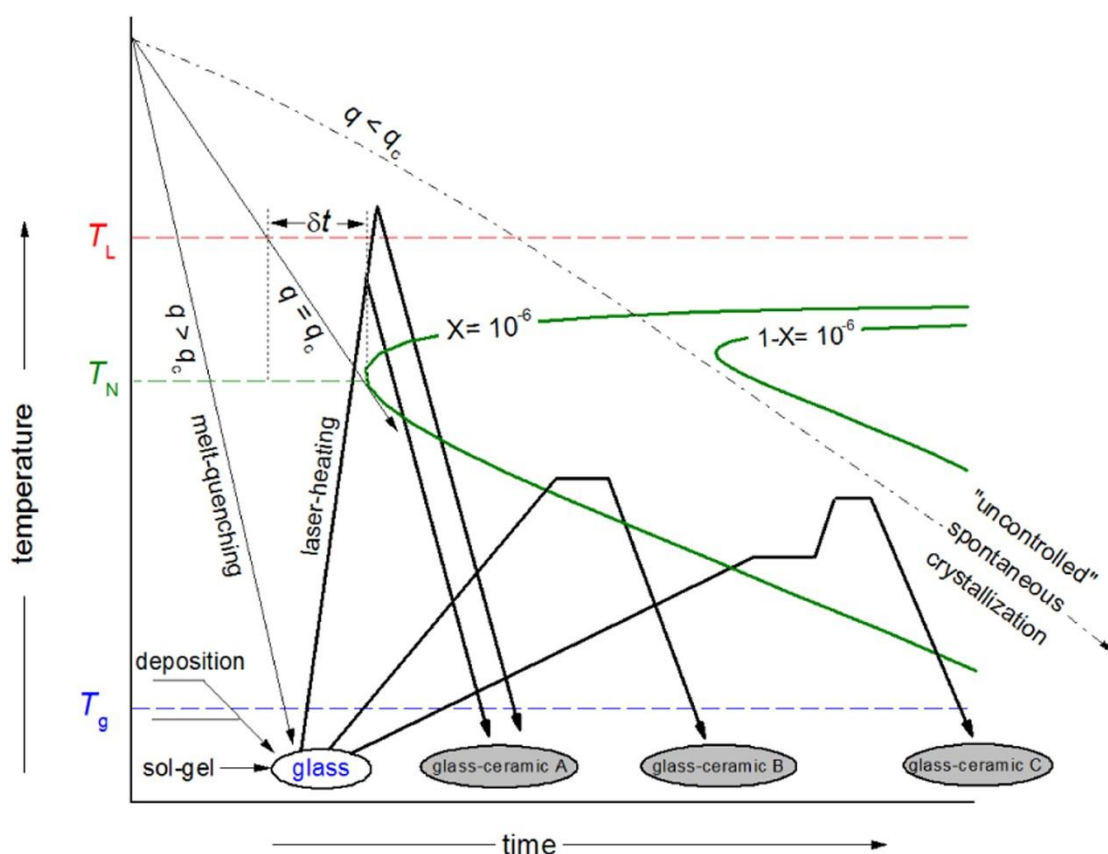


**Figure 9.** Schematic of conversion of glass into GCs. Reprinted with permission from Ref. [65].

### 3.2.1. Isothermal Treatment

It is not easy to make TGCs of specific crystals because the crystallization process may involve the simultaneous formation of different crystalline phases, especially for the parent glass with multiple components. Nucleation and crystal growth, which reach their maximum rates at different temperatures, are two separate processes. In general, the temperature of the maximum growth rate is 50–100 °C above the glass transition temperature ( $T_g$ ). When the critical dimension  $r^*$  is reached, the crystal will grow at the nucleation temperature. Nucleation stops when the temperature is raised beyond a certain range, and only a nucleus larger than  $r^*$  formed in the nucleation temperature range will further grow into larger crystals. Nucleation and growth processes can also occur simultaneously because their temperature ranges overlap greatly. Typically, nucleation and the growth of crystals occur simultaneously when GCs are synthesized using a one-step method (glass–ceramic B in Figure 9). Differently, the two-step method means that nucleation is followed by the growth of crystals (glass–ceramic C in Figure 9). Margha [66] prepared and stabilized the bismuth molybdate  $\beta$ - $\text{Bi}_2\text{Mo}_2\text{O}_9$  and monoclinic-scheelite  $\text{BiVO}_4$  phase in the  $\text{Bi}_2\text{O}_3$ - $\text{B}_2\text{O}_3$ - $(\text{MoO}_3 \text{ or } \text{V}_2\text{O}_5)$  system. The applied heat treatment program showed a significant effect on the size of the formed crystals, especially in samples with molybdenum content. Compared with two-step heat treatment (355 °C/1 h + 400 °C/2 h), one-step heat treatment (500 °C/2 h) has higher crystallinity. It is also noticeable that one-step heat treatment allows for more growth of the crystals than the two-step heat treatment. However, this will lead to overgrowth and coarsening of the crystals, which will cause the glass to lose its transparency. Two-stage isothermal treatment at two different temperatures is usually employed to separate nucleation and growth for better control over the growth of TGC crystals. In the presence of a sufficient number of nuclei, crystal growth is limited to obtain size-limited crystals, preferably less than 20 nm, to finally obtain TGC. Under this circumstance, crystal growth with only a few nuclei can form larger grains,

resulting in a partial loss of transparency. Certain glasses cannot induce nucleation even at temperatures of very low viscosity. Then, we can use heterogeneous nucleation to initiate crystallization of the glass at lower temperatures by adding nucleating agents such as  $\text{TiO}_2$ ,  $\text{ZrO}_2$  and noble metal nanoparticles.

### 3.2.2. Elemental Particle Precipitation

Precipitation of elemental particles in a glass matrix can be accomplished by thermal decomposition of unstable precursors or reduction with reducing agents to form elemental particles. At the melting temperature, the precursor salt (e.g.,  $\text{AgCl}$ ) is completely solvated, and then the precursor is reduced to form an atomically noble metal species. If atomic or molecular state elements are present in the glass melt, they may be in the quenched structure. During the subsequent heat treatment, these metal atoms aggregate, grow and form larger nanocrystals through atomic diffusion. That is to say, the desired metal species can be induced into the glass melt by addition of these metal species through raw materials or redox reactions. Lin et al. [57] used a metallic reducing agent (metallic Al) to reduce other metal or semiconductor oxides (for example,  $\text{GeO}_2$ ) to their atomic state (Ge) by melt-quenching processes (process 1 in Figure 10). During subsequent heat treatment (process 2 in Figure 10), this semiconducting element (Ge) will aggregate in the atomic state, grow and form nanocrystals by atomic diffusion inside the glass. This redox reaction can be carried out in a glass matrix: at the glass transition temperature, metal Al is completely dissolved in the glass grid, forming a homogeneous “solution” at high temperature, which can be quenched to form a colorless transparent glass. Utilizing the redox equilibrium established between the reducing agent and various oxides forms crystal nuclei in the melt quenching stage. During the subsequent heat treatment stage, the redox reaction leads to the reduction in the glass network and diffusion to grow nanoparticles on the nuclei (see Figure 10). The particle size can be well controlled by the heat treatment temperature and holding time—a higher reaction temperature favors the formation of crystalline particles with larger average particle size.

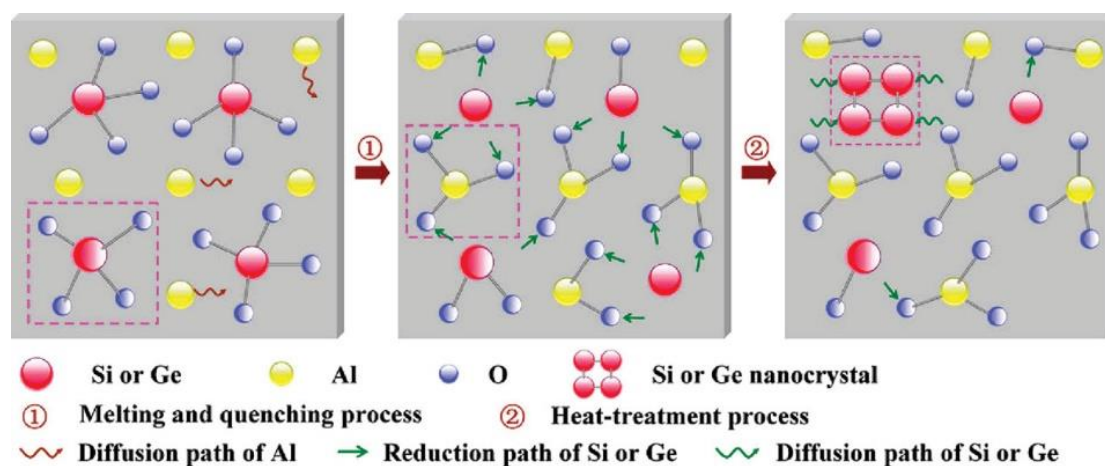


**Figure 10.** Schematic illustrations of the local transitions inside the glass composite. Reprinted with permission from Ref. [57].

### 3.2.3. Powder Sintering, Co-Melting and Frozen Sorbent Processes

These three methods have the following common characteristics: stable glasses cannot be formed directly from starting materials, and the raw materials are required to be processed through these processes to form TGCs. These methods allow us to obtain a GC with the desired crystalline phases easily.

Powder sintering techniques are more efficient and versatile than solid-state reaction because a larger number of fresh particle surfaces provides abundant nucleation sites. Crystal growth during powder sintering starts at the interface and then occurs in the

mostly glassy phase. The starting glass powder can be prepared by pulverizing molten tempered glass or by conventional sol-gel processes. Various low-melting glasses can serve as matrices with sufficient chemical stability, including borate and heavy metal oxide-based glasses [67]. Co-sintering of a mixture of low melting point glass powder and stable crystalline particles can incorporate the crystalline phase into the glassy matrix to obtain GC. The crystalline particles remain stable and insoluble in the glassy phase, and the glass powder softens and, eventually, densifies after sintering. When the melting temperature of ingredients in the raw materials is very different, and part of the components has good glass-forming ability, the powders of crystalline materials can be directly sintered at a designated temperature, producing crystalline GC composites in glass. For example, oxynitride GCs with high melting temperature cannot be prepared by melt quenching, but can be synthesized by sintering crystalline powder mixtures in an inert atmosphere [68,69]. In general, the transparency of powder sintered GCs is inferior compared to that obtained by melt-quenching and heat treatment. The optical transparency of GCs is lost due to the unavoidable scattering of pores and grain boundaries during sintering.

The co-melting process is a more direct method to produce GC in which glass components and pre-synthesized NCs are eutectic and then quenched to a GC. Compared to the traditional annealing process, this method allows more or almost limitless options for crystal-glass combinations. However, there are two factors to be considered when using this method: (1) the low melting point matrix glass is usually chosen to avoid the “dissolution” of NCs during melting [70,71]; (2) to ensure superior optical transparency, the refractive index difference between the crystal and glass phases has to be minimized [72–74].

The “frozen sorbent (FS) method” is used to fabricate GCs containing crystalline phases of high melting temperature. Unlike the two methods described previously, this process does not require a lengthy heat treatment process to precipitate crystals but prepares GC by quenching the melt with a component outside the glass-forming region [75–77]. For instance, GCs containing  $\beta$ -Ca<sub>2</sub>SiO<sub>4</sub> crystals can be prepared by quenching the melt with the composition of 60CaO-40SiO<sub>2</sub> from 1550 °C to room temperature. A homogeneous melt can only be obtained at temperatures above 1630 °C, while the melt at 1550 °C consists of a liquid phase and crystalline phase. Then, this kind of liquid–solid mixture is quenched to room temperature leading to formation of a composite consisting of the target crystal [77]. The state of a melt consisting of liquid and crystalline phases in a given composition is often determined in accordance with the equilibrium phase diagram, allowing for adjustments in composite design or control. According to Nakanishi et al., the advantages of this process include [75]: (1) the ability to prepare GCs containing metastable phases; (2) the possibility to obtain novel GCs with a high temperature crystal phase by referring to the phase diagram.

#### 3.2.4. Sol-Gel Process

The sol-gel method is a liquid phase process in which compounds containing high chemically active components are cured by solution, sol and gel and then heat-treated to form oxides or other solid compounds. Using inorganic substances or metal alkoxides as precursors, these raw materials are uniformly mixed in the liquid phase, and catalytic hydrolysis and condensation reactions are carried out to form a stable transparent sol system in the solution. The sol is further polycondensed and polymerized by aging to form a gel with a three-dimensional spatial network structure. Finally, molecular and even nanostructured materials are prepared from the gel by drying, sintering and solidifying. This process allows the formation of various glasses with special compositions (such as high-silica glasses) that cannot be achieved by ordinary fusion quenching methods under mild synthesis conditions. In many instances, these compounds can be replaced with common inorganic metal salts (such as nitrates and chlorides) and organic chelating agents, rather than expensive and volatile metal alkoxides or organic compounds. After a long period of careful gel aging and high temperature sintering densification process, a monolithic sol-gel glass is finally obtained [78,79].

Since the raw materials used in the sol-gel process are first dispersed in solvent to form a low-viscosity solution, molecular-level homogeneity can be achieved in a very short time. The glasses prepared through a sol-gel route are found to have advantages over the routine melted-quenching method, such as better homogeneity, higher level purity and lower stoichiometric losses [80–82]. Another significant advantage is the high flexibility of the composition of the prepared materials and the ease of application of the large substrate area [83,84]. Glasses containing nanoparticles can be transparent when the size of the nanoparticles is sufficiently smaller than the wavelength of light. Various monolithic transparent fully densified glasses containing nanoparticles have been prepared by the sol-gel method [82]. Zhou et al. [85] synthesized a  $\text{Er}_{3+}$  doped  $\text{SiO}_2$ - $\text{CaF}_2$  TGC by the sol-gel method. With an increasing heating temperature, the  $\text{CaF}_2$  nano-crystallites gradually grow up. The  $\text{CaF}_2$  crystallites in the sample heat-treated at  $900\text{ }^\circ\text{C}$  are 10–20 nm in size, distributed homogeneously among the amorphous silica matrix. The optical transmittance spectrum shows that the transmission of the sample is around 80% in the visible region.

The sol-gel method can also prepare various GCs more directly without the crystallization process by heat treatment. This is achieved by dispersing pre-synthesized NCs in a liquid sol, and the subsequent gelation process leads to the formation of solid gels containing dispersed NCs. This process allows for an almost limitless choice of crystals, as long as they remain stable during the sol and gel process. Introducing functional NCs into amorphous gels can greatly expand the applications of conventional silica and glass materials. Quantum dots (QDs) and different types of inorganic nanoparticles can be incorporated into silica gels through this sol-gel process without a crystallization precipitation process [86,87]. However, compared with ordinary GCs prepared by conventional methods, sol-gel composites are rarely studied in the field of photocatalysis.

### 3.2.5. Laser Induced Crystallization Techniques

Since the laser was invented in 1960, it has been contributing to the development of modern chemistry—particularly in molecular spectroscopy and photochemistry. Glass laser-induced crystallization is a new type of glass material crystallization technology, which can be used to precipitate crystals in a localized fashion either on the surface or the interior of the glasses. Actually, the precipitation of crystals in glass is not easy, since most oxide glasses, e.g., silicate glasses, are stable against crystallization at temperatures up to  $1000\text{ }^\circ\text{C}$ . In addition, optical glasses are transparent in the visible and near-infrared range (NIR), and the thermal effect induced by most continuous wave (CW) lasers operating in the visible/near-infrared range (NIR) is too weak to initialize crystallization of the glass. By incorporating active metal ion centers in the glass, the absorption of the metal ion centers induces significant localized heating, leading to crystalline precipitation inside glass or on the glass surface.

An oxide glass with the composition (mol%) of  $10\text{RO}-10\text{Sm}_2\text{O}_3-80\text{TeO}_2$  ( $\text{R} = \text{Mg}$  or  $\text{Ba}$ ) was obtained by Komatsu et al. [88] for the first CW laser induced crystallization. After irradiation of a CW YAG:Nd laser at 1064 nm for 30 s, a dot pattern with a diameter of about 50–150  $\mu\text{m}$  can be generated, which induced the change of refractive index. This laser crystallization method was later extended to “write” different crystalline patterns on glass surfaces, using rare earth ions such as  $\text{Sm}^{3+}$  and  $\text{Dy}^{3+}$  as the absorbers for the NIR laser [89–91]. In the recent decade, different lasers have been used to craft crystalline patterns in/inside glasses of diverse compositions and to fabricate optical waveguide by taking advantage of the induced change in refractive index [92].

Compared with the CW laser, pulse lasers offer higher peak power and better spatial resolution in glass microfabrication. The structure of selected points in glasses can be modified by laser irradiation [93]. Focusing intensive laser pulses into the bulk of a transparent material is a novel technique that has been used to modify the irradiated area. Depending on the laser conditions, the induced changes are different. Parameters such as laser power and scanning speed have an effect on the size and density of the crystal spot. Sufficiently high laser pulse intensities can produce a local redistribution

of the glass structure and major permanent modifications of the microstructure and its properties. The result of this laser treatment is a change in the physical and chemical properties of the irradiated area, such as transparency, refractive index, etc. With the rapid development of ultrafast laser technology in recent decades, nanosecond (ns), picosecond (ps) and femtosecond (fs) lasers have been extensively used in microstructure fabrication. These lasers, especially the fs laser, enable direct fabrication of microstructure in a sub-micrometer scale, facilitating a wide range of applications in diverse areas. Ultrafast laser direct writing-based glass crystal optics has been widely reported to realize 3D nonlinear photonic crystals [94,95], second harmonic generation [96,97], optical waveguides [98,99] and perovskite quantum dots in the glass [100,101]. Femtosecond lasers are more universal to material micropatterning, including the crystallization of glass. Compared to other pulsed laser systems, fs lasers offer unprecedented peak power density, and the use of the fs laser for microfabrication exerts minimal thermal effect on the materials, thus providing high spatial resolution. More importantly, the fs laser allows the precipitation of 3D crystalline patterns or microstructures in a transparent glass, which is not easily achieved by most other types of lasers. The first SHG crystal precipitated from glass using an fs laser was originated by Miura et al. [102] in a parent glass of  $47.5\text{BaO}-5\text{Al}_2\text{O}_3-47.5\text{B}_2\text{O}_3$ .

In a word, the most important thing for the design and preparation of PGCs is to properly control the transparency and crystallinity of GCs. On the one hand, it is difficult for most GCs to obtain high transparency due to the difference of refractive index between nanocrystals and the glass matrix. On the other hand, the excessive growth and coarsening of crystals will lead to the prominent Mie scattering effect. In addition, it is highly desirable to obtain surface crystallization of PGCs by various means of controlled crystallization. Low photocatalytic activity limits the wide application of GCs, especially under visible light or solar irradiation, and thus, a great deal of effort still needs to be invested in the development of PGC materials with improved properties. It has been experimentally proved that higher crystallinity of PGC materials possesses better photocatalytic activity. However, higher crystallinity of PGC materials means overgrowth and coarsening of the crystals, which will cause the glass to lose its transparency. Furthermore, the higher crystallinity of PGC materials easily results in macro and micro defects such as cracks, vacancies, dangling bonds at the interface between precipitated crystals and residual glass matrix, which evidently decreases not only the transparency but also photocatalytic efficiency. From the transparency and crystallinity (photocatalytic activity) points of view, there is strong conflict between them; thereby, how to balance the crystallinity (photocatalytic activity) and transparency is very critical to preparation and widely application of transparent photocatalytic glass ceramics.

#### 4. Modification Strategies of PGCs

Given the various limitations of photocatalysts in powder or thin film form, researchers have proposed glass-based materials, which could be a good option and can play a vital role due to easy control of properties, low-cost scale-up possibilities and lower maintenance [103]. However, the inefficient utilization of visible light and the rapid recombination of the photogenerated electrons and holes are often two major limiting factors which inhibit the improvement of photocatalytic activity. Generally, different strategies were employed to enhance its photocatalytic activity, including chemical etching, doping with rare earth metals, non-metallic or metal dopants, etc. [104–106] Table 1 summarizes and compares the photocatalytic properties of various reported GCs.

**Table 1.** Various reported PGCs and their performances.

Composition Name	Crystallization Method	Major Crystalline Phases	Light	Photocatalysis Experiment	Performance Achieved	Ref.
CaO–BaO–B <sub>2</sub> O <sub>3</sub> –Al <sub>2</sub> O <sub>3</sub> –TiO <sub>2</sub> –ZnO	HT	TiO <sub>2</sub>	UV	Escherichia coli degradation	10 h ~95% bacterial cells degraded	[44]
20P <sub>2</sub> O <sub>5</sub> –75TiO <sub>2</sub> –2Al <sub>2</sub> O <sub>3</sub> –3(Na <sub>2</sub> O, MgO)	HT	TiO <sub>2</sub>	UV	MB dye degradation	120 min ~100% dye degraded	[7]
9TiO <sub>2</sub> –31P <sub>2</sub> O <sub>5</sub> and 76TiO <sub>2</sub> –24P <sub>2</sub> O <sub>5</sub>	HT	TiO <sub>2</sub>	UV	MB dye degradation	120 min ~55% dye degraded	[45]
CaO–B <sub>2</sub> O <sub>3</sub> –Bi <sub>2</sub> O <sub>3</sub> –Al <sub>2</sub> O <sub>3</sub> –TiO <sub>2</sub>	HT	TiO <sub>2</sub>	UV	MB dye degradation	K = 0.59 h <sup>-1</sup> m <sup>-2</sup> degraded	[107]
4CaO–64B <sub>2</sub> O <sub>3</sub> –9BaO–9ZnO–Al <sub>2</sub> O <sub>3</sub> –14TiO <sub>2</sub>	HT	TiO <sub>2</sub>	UV	MB dye degradation	k = 0.78 h <sup>-1</sup> .m <sup>-2</sup> degraded	[108]
SiO <sub>2</sub> –Al <sub>2</sub> O <sub>3</sub> –B <sub>2</sub> O <sub>3</sub> –CaO–TiO <sub>2</sub>	HT/ E-HNO <sub>3</sub>	TiO <sub>2</sub>	UV	MB dye degradation	20 hr 20 μmol dye degraded	[43]
14TiO <sub>2</sub> –23ZnO–45B <sub>2</sub> O <sub>3</sub> –18Al <sub>2</sub> O <sub>3</sub> –4.5SiO <sub>2</sub>	E-HCl	TiO <sub>2</sub>	UV	H <sub>2</sub> evolved	1.09 μmol/h H <sub>2</sub> evolved	[109]
0.4BaO–0.4TiO <sub>2</sub> –B <sub>2</sub> O <sub>3</sub>	HT	TiO <sub>2</sub>	Visible	Bacterial degradation	120 min ~98.3% bacteria degraded	[110]
12MgO–48TiO <sub>2</sub> –31P <sub>2</sub> O <sub>5</sub> –9SiO <sub>2</sub>	HT	MgTi <sub>4</sub> (PO <sub>4</sub> ) <sub>6</sub>	UV	MB dye degradation	27–32 nmol/L/min dye	[46]
9.35K <sub>2</sub> O–9.35CaO–42.05ZnO–23.36B <sub>2</sub> O <sub>3</sub> –9.35SiO <sub>2</sub> –6.54Al <sub>2</sub> O <sub>3</sub>	HT	ZnO	UV	(rhodamine b) RB dye degradation	150 min ~78.57% dye degraded	[48]
SiO <sub>2</sub> –TiO <sub>2</sub> –ZnO–B <sub>2</sub> O <sub>3</sub> –Na <sub>2</sub> O–K <sub>2</sub> O–P <sub>2</sub> O <sub>5</sub> –Li <sub>2</sub> O–BaO	HT	ZnO	UV	Red SPD Cotton dye degradation	275 min ~76% dye degraded	[47]
WO <sub>3</sub> –ZnO–B <sub>2</sub> O <sub>3</sub>	HT/ E-HNO <sub>3</sub>	α-ZnWO <sub>4</sub>	UV and Visible	MB dye degradation	180 min ~100% dye degraded	[111]
2Bi <sub>2</sub> O <sub>3</sub> –B <sub>2</sub> O <sub>3</sub>	HT	Bi <sub>4</sub> B <sub>2</sub> O <sub>9</sub>	UV	17 β-estradiol (pharmaceutical) degradation	240 min ~80% β-estradiol degraded	[62]
2Bi <sub>2</sub> O <sub>3</sub> –B <sub>2</sub> O <sub>3</sub>	E-HF	BiO <sub>0.1</sub> F <sub>2</sub> , BiF <sub>3</sub>	Visible	Rhodamine 6G dye degradation	120 min ~85% dye degraded	[112]
2Bi <sub>2</sub> O <sub>3</sub> –B <sub>2</sub> O <sub>3</sub>	E-HCl	BiOCl	UV	MB dye degradation	180 min ~100% dye degraded	[113]
SrO–Bi <sub>2</sub> O <sub>3</sub> –B <sub>2</sub> O <sub>3</sub>	HT	SrBi <sub>2</sub> B <sub>2</sub> O <sub>7</sub>	UV	MB dye degradation	540 min ~50% dye degraded	[63]
SrO–Bi <sub>2</sub> O <sub>3</sub> –B <sub>2</sub> O <sub>3</sub>	E-HF	BiOF/α-BiF <sub>3</sub>	UV	MB dye degradation	540 min ~90% dye degraded	[114]
SrO–Bi <sub>2</sub> O <sub>3</sub> –B <sub>2</sub> O <sub>3</sub>	E-HCl	SrBi <sub>2</sub> B <sub>2</sub> O <sub>7</sub>	UV	MB dye degradation	4 h ~100% dye degraded	[115]
ZnO–Bi <sub>2</sub> O <sub>3</sub> –B <sub>2</sub> O <sub>3</sub>	ZnO–Bi <sub>2</sub> O <sub>3</sub> –B <sub>2</sub> O <sub>3</sub>	BiOCl/BiF <sub>3</sub>	UV	MB dye degradation	225 min ~90% dye degraded	[116]
(70B <sub>2</sub> O <sub>3</sub> –29Bi <sub>2</sub> O <sub>3</sub> –1Dy <sub>2</sub> O <sub>3</sub> )–x(BaO–TiO <sub>2</sub> )	HT	Ba <sub>2</sub> Ti <sub>6</sub> O <sub>13</sub>	UV	Ciprofloxacin degradation	268 min <sup>-1</sup> m <sup>-2</sup>	[117]
xCaCu <sub>3</sub> Ti <sub>4</sub> O <sub>12</sub> –(100–x) TeO <sub>2</sub> (x = 0.25 to 3 mol%)	HT	TiTe <sub>3</sub> O <sub>8</sub> , CaTiO <sub>3</sub>	Visible	H <sub>2</sub> evolved	135 μmol h <sup>-1</sup> g <sup>-1</sup> H <sub>2</sub> evolved	[118]
15Na <sub>2</sub> O–15CaO–40Fe <sub>2</sub> O <sub>3</sub> –xAl <sub>2</sub> O <sub>3</sub> –(30–x)SiO <sub>2</sub>	HT	Ca <sub>2</sub> Fe <sub>22</sub> O <sub>33</sub> , CaFe <sub>2</sub> O <sub>4</sub>	Visible	MB dye degradation	K = 9.26 × 10 <sup>-3</sup> min <sup>-1</sup> degraded	[119]
Fe <sub>2</sub> O <sub>3</sub> –Bi <sub>2</sub> O <sub>3</sub>	HT, E-HF, HNO <sub>3</sub>	β/γ-Bi <sub>2</sub> O <sub>3</sub> , BiFeO <sub>3</sub>	Visible	RY160 dye degradation	120 min ~99% dye degraded	[120]
52SiO <sub>2</sub> –10Na <sub>2</sub> O–6MgO–6B <sub>2</sub> O <sub>3</sub> –12K <sub>2</sub> O–10ZnO–4TiO <sub>2</sub>	HT	Bi <sub>2</sub> S <sub>3</sub> quantum dots	solar light	H <sub>2</sub> evolved	6418.8 μmole h <sup>-1</sup> g <sup>-1</sup>	[121]
Er <sup>3+</sup> /Yb <sup>3+</sup> –CaO–Al <sub>2</sub> O <sub>3</sub> –SiO <sub>2</sub> –CaF <sub>2</sub>	HT	TiO <sub>2</sub> /CaF <sub>2</sub>	NIR	MO dye degradation	Not mentioned	[122]
Er <sup>3+</sup> /Yb <sup>3+</sup> /Y <sup>3+</sup> –SrO–Bi <sub>2</sub> O <sub>3</sub> –B <sub>2</sub> O <sub>3</sub>	HT	BiOCl/SrF <sub>2</sub>	NIR	Norfloxacin degradation	90 min 66% NOR and 79% methyl orange degraded	[123]
Er <sup>3+</sup> /Yb <sup>3+</sup> –SrO–Bi <sub>2</sub> O <sub>3</sub> –B <sub>2</sub> O <sub>3</sub>	HT	BiOCl/SrF <sub>2</sub>	NIR	Norfloxacin degradation	90 min 98% NOR degraded	[124]
Yb <sup>3+</sup> /Tb <sup>3+</sup> –SrF <sub>2</sub> –Bi <sub>2</sub> O <sub>3</sub> –B <sub>2</sub> O <sub>3</sub>	HT	BiOBr/SrF <sub>2</sub>	NIR	Norfloxacin degradation	90 min 99% NOR degraded	[125]
Er <sup>3+</sup> /Yb <sup>3+</sup> –SrF <sub>2</sub> –Bi <sub>2</sub> O <sub>3</sub> –B <sub>2</sub> O <sub>3</sub> –V <sub>2</sub> O <sub>5</sub>	HT	Bi <sub>1.95</sub> Yb <sub>0.04</sub> Er <sub>0.01</sub> V <sub>2</sub> O <sub>8</sub>	NIR	Norfloxacin degradation	90 min 55.2% NOR degraded	[126]
Er <sup>3+</sup> /Yb <sup>3+</sup> –SrCO <sub>3</sub> –Bi <sub>2</sub> O <sub>3</sub> –B <sub>2</sub> O <sub>3</sub> –TiO <sub>2</sub>	HT	Sr <sub>2</sub> Bi <sub>4</sub> Ti <sub>4</sub> O <sub>15</sub> , SrTiO <sub>3</sub>	NIR	Norfloxacin degradation	90 min 86% NOR degraded	[127]

#### 4.1. Chemical Etching

For photocatalytic applications of glass and GCs, only surface crystallization is desirable. Generally, surface/bulk crystallization is governed by crystallization kinetics. To achieve surface crystallization, some of the advanced techniques such as ultrasonic treatment and laser-based heating can be selected, which are either cumbersome or expensive [128,129]. Thus far, numerous studies have shown that fluorination treatment is beneficial to improve the photocatalytic performance of Bi-based compounds [130–133]. The fluorination enhances the interfacial charge transfer dynamics for better surface adsorption. In addition, fluorination can also reduce the grain size and change the band gap.

Sharma et al. [112] prepared  $2\text{Bi}_2\text{O}_3\text{-B}_2\text{O}_3$  (BBO) GCs by wet etching with different concentrations of hydrofluoric acid (HF) aqueous solution (HF; concentrations used: 3, 6, and  $12\text{ mol}\cdot\text{L}^{-1}$ ). The corrosion of HF aqueous solution led to the formation of  $\text{BiF}_3$  and  $\text{BiO}_{0.1}\text{F}_{2.8}$  phases. Etching of glass samples showed more evolution peaks with increasing HF concentration in aqueous solution and could lead to the formation of a visible-light active  $\text{BiF}_3$  phase. For as-quenched glass samples, the direct band gap was 2.47 eV, while the etched samples, viz. BBO HF1, BBO HF2 and BBO HF3, attained values of 4.02 eV, 3.81 eV and 3.64 eV, respectively. The photocatalytic degradation of rhodamine 6G (Rh 6G) dye under visible light irradiation within 120 min is shown in Figure 11. Enhanced visible light-driven photocatalytic activity was observed in HF etched GCs compared to the as-quenched BBO glass, and the degradation rate of Rh 6G by BBO HF3 glass samples can reach up to 85%. The photocatalytic activity increases with the increase in HF concentration, which is due to the formation of the  $\text{BiF}_3$  phase and the sharp increase in surface roughness value by the etching of high-concentration HF solution. Contact angle of the as-quenched glass was  $90.2^\circ$ , which could be reduced to  $20.02^\circ$  with the increase in the HF concentration in the etching solution. This hydrophilic nature of the etched glass samples is favorable for the photocatalytic performance because the water droplets can cover a larger portion of the surface for wiping out the pollutants. Such photo-induced hydrophilicity and catalytic properties make translucent GCs promising for self-cleaning and waste water treatment applications. Simply via surface fluorination of  $\text{SrO-Bi}_2\text{O}_3\text{-B}_2\text{O}_3$  (SBBO) GC, by using HF solution, Singh et al. [114] obtained the coating of cubic  $\text{BiO}_{0.51}\text{F}_{1.98}$  over SBBO GC similarly. Figure 12 shows a focused SEM image of as-quenched SBBO GC and fluorinated SBBO GCs. SBBO-HF-2 contains small spheres with diameters in the 40–80 nm range, including cubic clusters in addition to small spherical particles, but more fluorination will reduce spheres with diameters between 50 and 100 nm. Under the maximum fluorination, large cubes with a size of 150 nm to 250 nm are displayed, with a small number of agglomerated particles between 10 and 20 nm distributed between these cubes. With the continuous fluorination of concentrated HF solution, the crystal structure of the coating tends towards the cubic  $\alpha\text{-BiF}_3$  structure from the cubic  $\text{BiO}_{0.51}\text{F}_{1.98}$ . The structures of cubic  $\text{BiO}_{0.51}\text{F}_{1.98}$  and cubic  $\alpha\text{-BiF}_3$  have completely different morphologies, with the former having compact spheres and the other being densely packed cubes, respectively. With HF fluorination, the glass goes from transparent to translucent and then again to transparent; the unique process is due to the reduction in the refractive index difference between the growing crystal and the residual glass. The high transparency after fluorination may be due to the controlled homogeneous nucleation and growth of cubic  $\alpha\text{-BiF}_3$  crystals. The research group of Edgar D. Zanotto [134] expressed that, with further fluorination, the high transparency of the cubic crystallized glass is due to the simultaneous change in the composition of the glass matrix and crystals during the crystallization process, so that the respective refractive indices do not change considerably and remain almost similar to glass. The reaction rate constants for the degradation of MB corresponding to as-quenched and fluorinated SBBO-HF-1 (etched with 1.5 M HF), SBBO-HF-2 (etched with 3 M HF), SBBO-HF-3 (etched with 6 M HF) and SBBO-HF-4 (etched with 12 M HF) GCs were 0.00292, 0.01509, 0.02226, 0.01607 and  $0.01451\text{ min}^{-1}$ , respectively (Figure 12f). The fluorinated SBBO GC had more adsorption of MB than as-quenched SBBO GC, which was due to the increased surface

roughness. The relatively rapid drop in the  $C_t/C_0$  curve and increasing photocatalytic reaction rate from SBBO to SBBO-HF-2 are due to the reduction in the particle size and bandgap E1 of  $\text{BiO}_{0.51}\text{F}_{1.98}$  along with structural transformation to cubic  $\alpha\text{-BiF}_3$ . However, after further fluorination, the photocatalytic reaction rates of SBBO-HF-3 and SBBO-HF-4 decreased, respectively. Due to the increased relative hydrophobic properties of SBO-HF-3 and SBO-HF-4 GCs, further fluorination resulted in a relatively slow decrease in  $C_t/C_0$  and photocatalytic reaction rate.

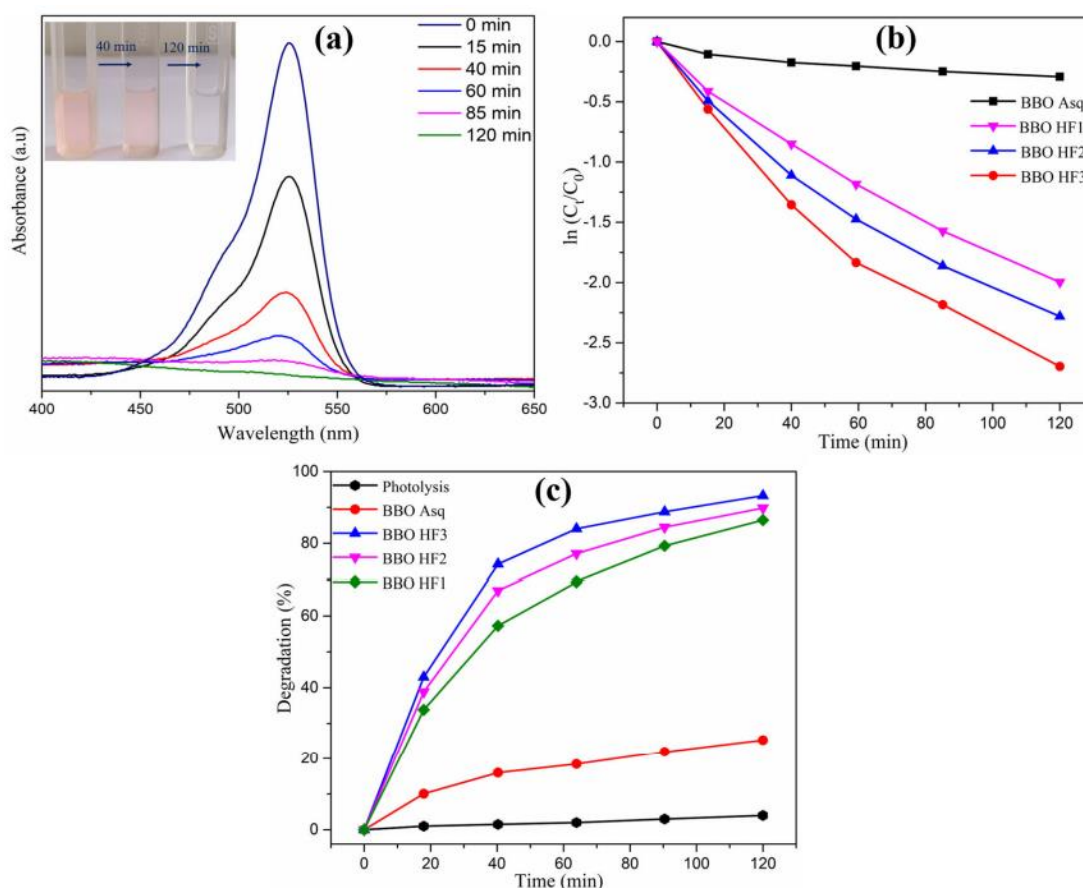


**Figure 11.** (a) Absorption spectra of Rh 6G degradation for BBO HF<sub>3</sub> glass sample. (b) Photodegradation curves of as-quenched and HF-etched glass samples. (c) Degradation percentage of as-quenched and HF-etched glass samples. Reprinted with permission from Ref. [112].

In the same way, a similar effect can be obtained by etching the surface with HCl. Yoshida et al. [109] proposed a unique and novel method to achieve surface crystallization. The fabrication principle is very simple, that is, using acid to etch glass at room temperature to achieve surface crystallization. The results show that the etched sample has 16 times higher activity of  $\text{H}_2$  generation than that of the non-etched one.  $\text{TiO}_2$  nano-particles at the surface of the crystallized glass were precipitated by chemical etching, and the specific surface area improved. Sharma et al. [113] also achieved crystallization of the  $\text{BiOCl}$  structure over the  $2\text{Bi}_2\text{O}_3\text{-B}_2\text{O}_3$  (BBO) glass surface by HCl chemical etching and studied its photocatalytic response. Scanning electron microscopy revealed that large numbers of elongated plates or nanosheets grew on the glass' surface due to etching. These nanosheets cross each other to form a network-like porous hierarchical structure, similar to the morphology of flowers (Figure 13). During the etching process, Bi in the BBO composition was dissolved in HCl by following the Thomson–Freundlich formulation. In HCl solution, the  $\text{Bi}^{3+}$  ion reacts with the  $\text{Cl}^-$  ion and, hence, creates  $\text{BiCl}_3$ , which immediately hydrolyzes with  $\text{H}_2\text{O}$

(Equations (4) and (5)) and creates the polarized structure of BiOCl bonded with strong forces in a layered arrangement of “-(Cl-Bi-O-Bi-Cl)-”:

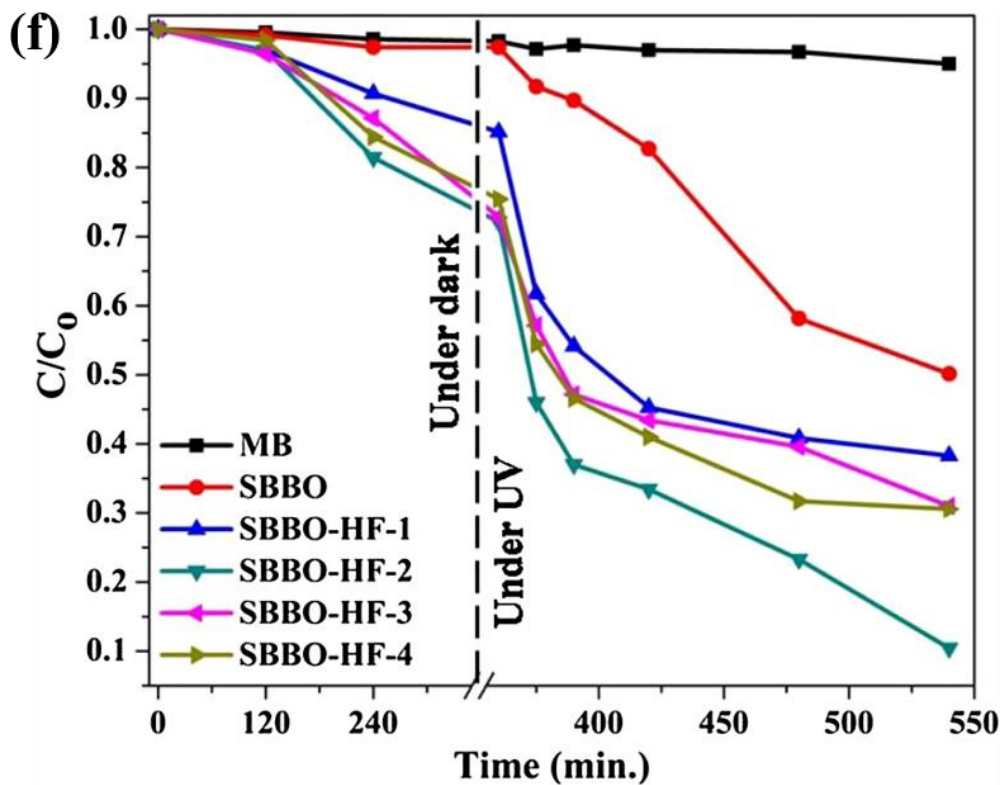
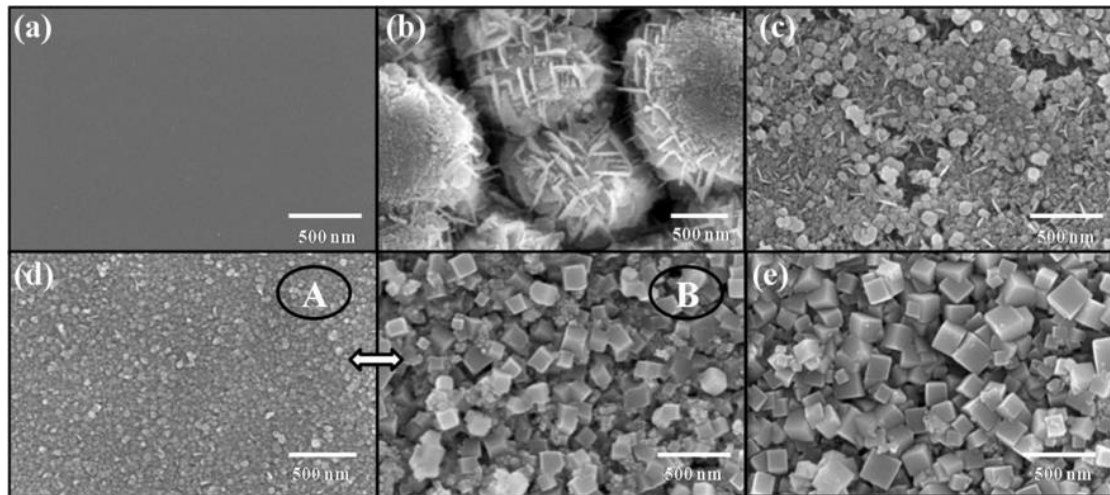


**Figure 12.** Focused SEM images of (a) as-quenched SBBO GC and etched SBBO GCs from HF solutions of different concentrations named as (b) SBBO-HF-1, (c) SBBO-HF-2, (d) SBBO-HF-3 (showing two different highlighted regions A and B) and (e) SBBO-HF-4, respectively. (f) The  $C_t/C_0$  curves for the adsorption–desorption of MB solution under dark and photocatalysis degradation under 420 nm irradiation for as-quenched and HF etched SBBO GCs with different concentration solutions. Reprinted with permission from Ref. [114].

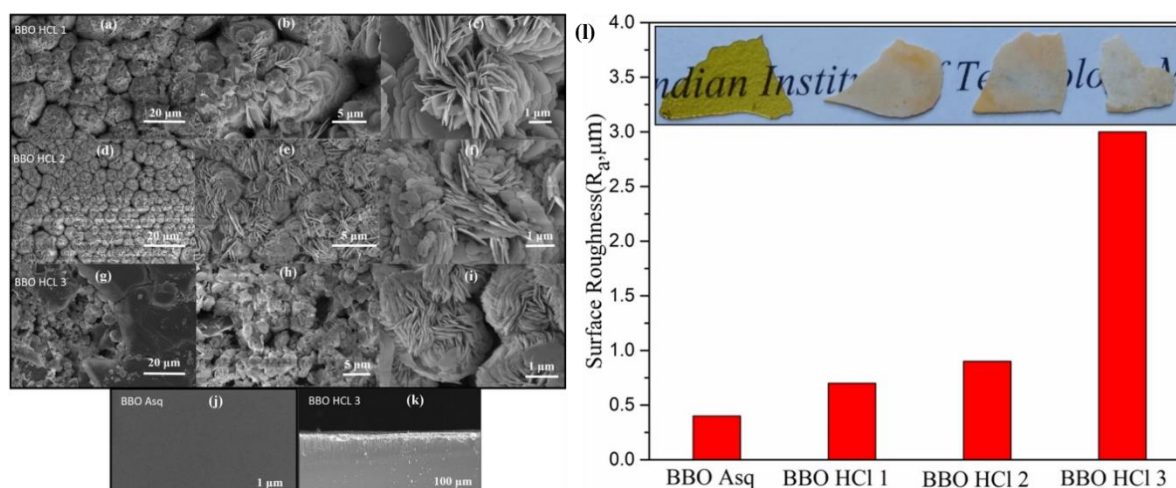


**Figure 13.** SEM images of (a–i) BBO HCl etching samples, (j) BBO as-quenched samples and (k) a typical cross-sectional image of the BBO HCl 3. (l) Surface roughness and images of BBO glass samples. Reprinted with permission from Ref. [113].

This arrangement stacks layer by layer along the *c* axis with weak interlayer van der Waals interactions [135]. The layer by layer and alternate stacking sequence of “-(Cl-Bi-O-Bi-Cl)-” along the (001) plane lead to semicircular plates/petals and automatically assemble as the flower- or cabbage-like structures. Increasing the concentration of HCl for etching of BBO creates pores as well as cracks, which increases the surface roughness, but excessive etchings with HCl decreased the transparency of the BBO, and its color changed from yellow to white, respectively (Figure 13l). Therefore, the etching process needs to be optimized to obtain better transparency and superior photocatalytic performance. A typical schematic diagram for the degradation of pollutants by HCl-etched BBO GCs under UV light irradiation is shown in Figure 14. Due to the absorption of photons with energy greater than or equal to the energy of the material, an electron is excited from the valence band to the conduction band, thereby forming an electron pair and a positive hole. These photoinduced positive holes and electrons undergo a series of reactions and finally produce hydroxyl ( $\cdot\text{OH}$ ) radicals and superoxide radicals ( $\cdot\text{O}_2^-$ ). An HCl-etched BBO GC is irradiated with ultraviolet rays; with the help of superoxide ions as well as hydroxyl radicals, the harmful pollutants are reduced to harmless products. Photocatalytic experiments on BBO glass samples etched with different concentrations of HCl showed that the degradation rate of methylene blue by BBO HCl3 glass was the highest, reaching almost 100% within 180 min. With the further increase in HCl concentration, the penetration depth in the glass sample increases, and more and more nucleation sites are formed, which further promotes the growth of BiOCl. BiOCl grows and is densely arranged along the (110) plane to form the flower-like hierarchical structure assembled with petals, which is conducive to absorbing the best solar radiation and reducing annihilation rate of electron and hole so as to obtain the best kinetic rate of photocatalytic reaction.

Singh et al. [115] also used HCl chemical etching to obtain the BiOCl layered structure over the SrO-Bi<sub>2</sub>O<sub>3</sub>-B<sub>2</sub>O<sub>3</sub> (SBBO) TGC. The schematic diagram is shown in Figure 15. Step 1 illustrates the distribution of SrBi<sub>2</sub>B<sub>2</sub>O<sub>7</sub> nano-sized crystals on the surface of the SBBO GC due to the optimization of melting and quenching temperatures. Step 2 is SBBO BiOCl-1 GC formed by etching SBBO GC by HCl, showing a network of triangle and quadrilateral cross-sections of semicircular plates. With the etching of SBBO GC, HCl reacts with Bi in SrBi<sub>2</sub>B<sub>2</sub>O<sub>7</sub> existing on the surface of the SBBO GC. Further increasing the etched HCl concentration, the dissolution of SrBi<sub>2</sub>B<sub>2</sub>O<sub>7</sub> and the recrystallization of the BiOCl semicircle plate occur simultaneously, and the flower’s morphology is assembled by a large number of ultra-long plates or nanosheets, as shown in Steps 3 and 4. The positively charged Bi<sup>3+</sup> ions in the SrBi<sub>2</sub>B<sub>2</sub>O<sub>7</sub> compound react with Cl<sup>-</sup> ions in HCl solution to form BiCl<sub>3</sub>.

Immediately,  $\text{BiCl}_3$  hydrolyzes with water and forms a  $\text{BiOCl}$  polarized structure. The four O atoms and four Cl atoms are attached tetragonally in opposite directions with Bi and construct asymmetric decahedral layered geometry along the c axis, shown in Step 5 [136]. These structures attached along the (001) plane in the stacking order of  $-(\text{Cl-Bi-O-Bi-Cl})-(\text{Cl-Bi-O-Bi-Cl})-(\text{Cl-Bi-O-Bi-Cl})-$ . They form semicircular plates/petals, flowers or cabbage and other layered structures in SBBO GCs etched with different concentrations of HCl. Therefore, the kinetic rate of degradation of MB for respected SBBO- $\text{BiOCl}$  GCs increases with the increase in the concentration of SBBO etched by HCl. Their team also achieved the controlled crystallization on the surface of  $\text{ZnO-Bi}_2\text{O}_3\text{-B}_2\text{O}_3$  glass via etching using HCl/HF, respectively [116]. Using four different concentrations of acid (3, 6, 9 and 12 M), different amounts of  $\text{BiOCl}$  and  $\text{BiF}_3$  surface crystals were obtained. As reported by Sharma [113], the morphology of the glass samples changed from plate-shaped particles to flower-shaped particles with the increasing concentration of etching acid. Additionally, the transparency was decreased with an increase in the concentration of acid used for etching owing to the increase in glass surface roughness. Compared with  $\text{BiF}_3$  surface-crystallized glass,  $\text{BiOCl}$  surface-crystallized glasses have more efficient photocatalytic performance. Under ultraviolet irradiation (UV), methylene blue was completely degraded by a  $\text{BiOCl}$  crystallized sample within 225 min, while maximum 90% degradation was achieved in a  $\text{BiF}_3$  crystallized sample, even after 300 min (Figure 16). It is due more to the narrow band gap values of  $\text{BiOCl}$  than those of  $\text{BiF}_3$  and also due to the presence of an internal electric field in the  $\text{BiOCl}$  layered structure, which prevents electron-hole pair re-combinations. The superior self-cleaning properties of  $\text{BiOCl}$  crystallized glasses were mainly due to the enhanced hydrophobicity of  $\text{BiOCl}$  crystallized glass compared with  $\text{BiF}_3$  crystallized glass.

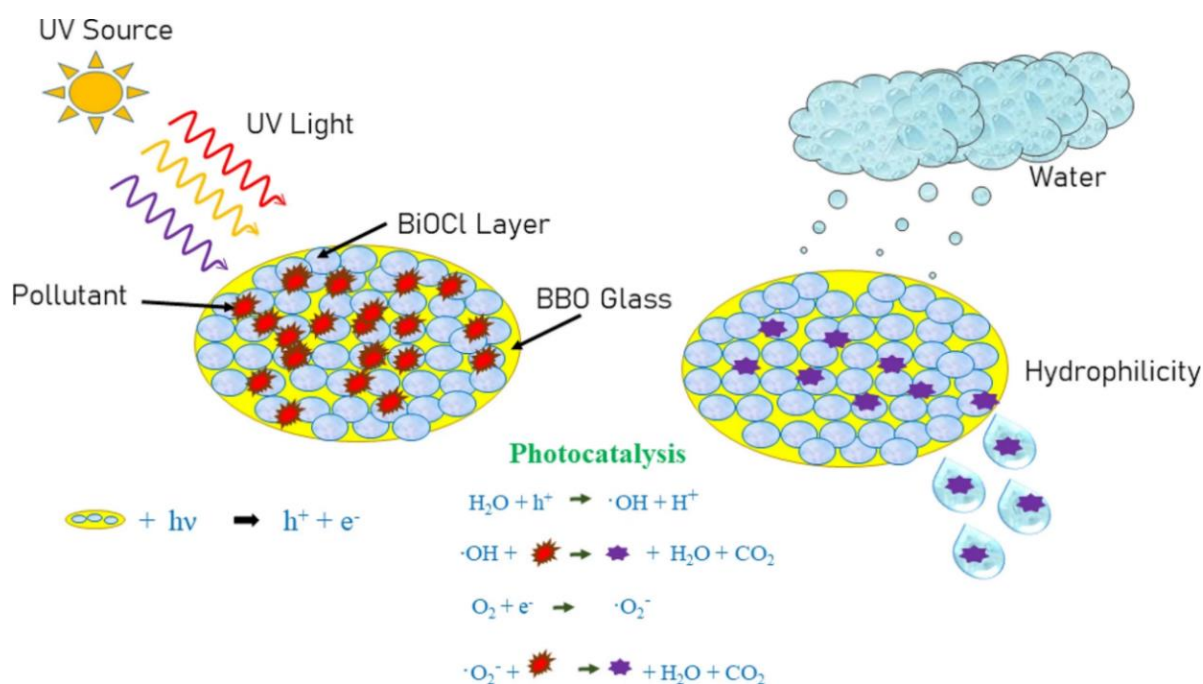


**Figure 14.** Schematic diagram of the mechanism for the photocatalytic degradation of pollutants under UV light irradiation. Reprinted with permission from Ref. [113].

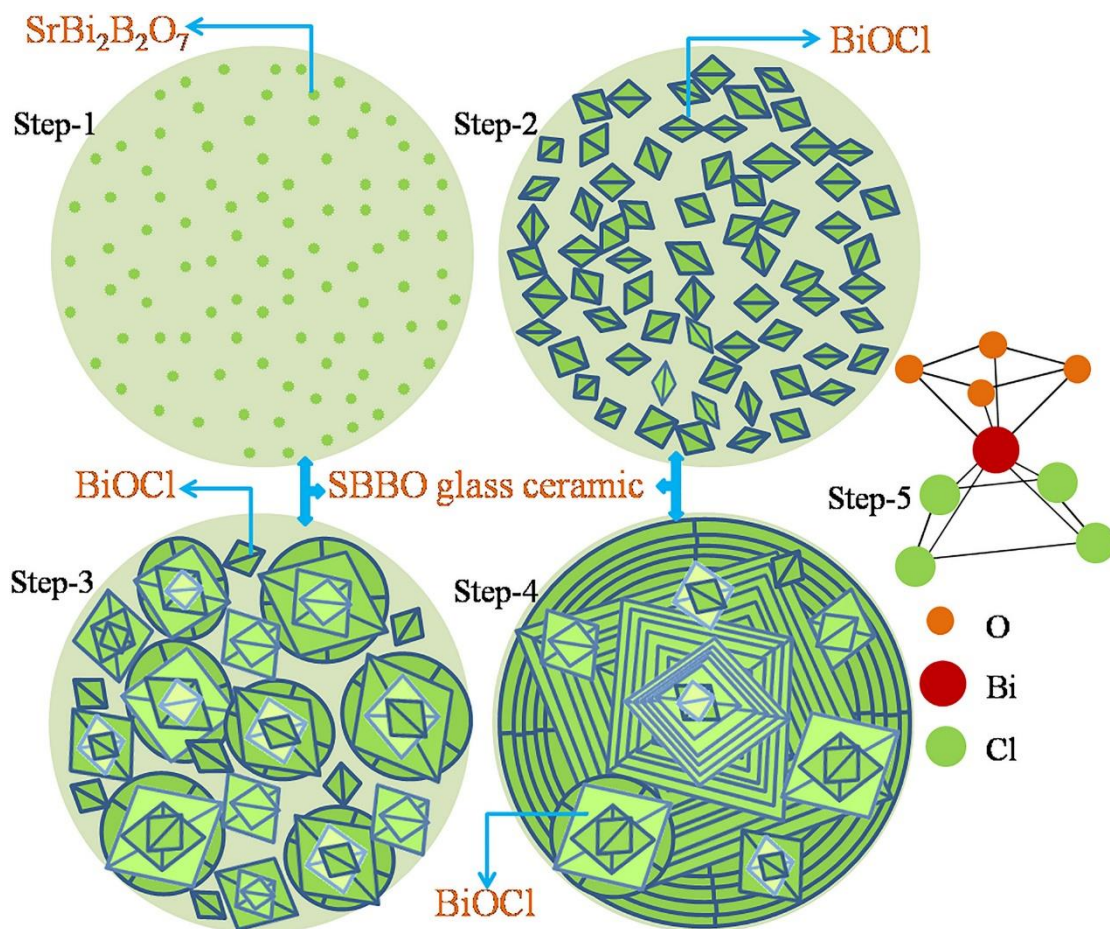


Figure 15. Schematic diagram of the growth of BiOCl over SBBO GC after etching by HCl solutions. Reprinted with permission from Ref. [115].

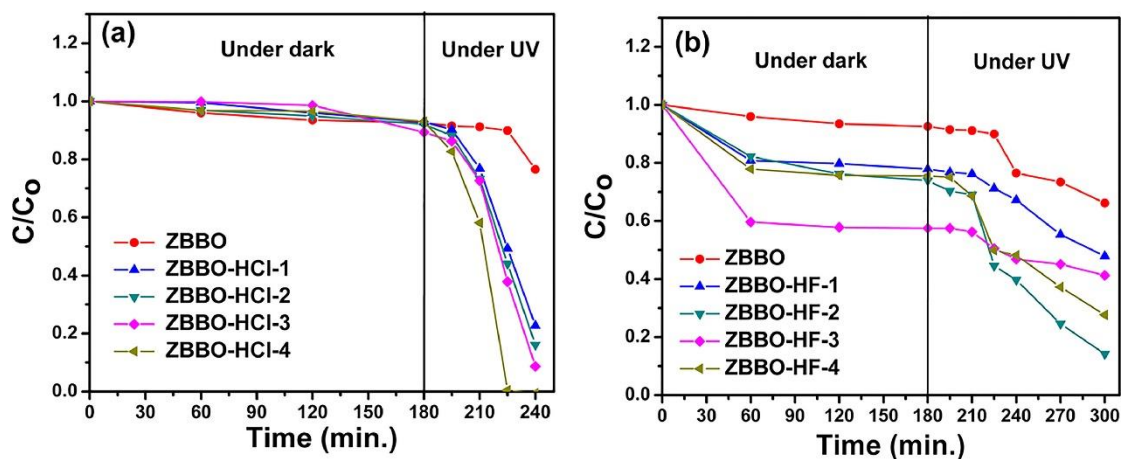


Figure 16.  $C/C_0$  vs. time plots obtained for (a) BiOCl-crystallized and (b) BiF<sub>3</sub>-crystallized glass samples during a methylene blue (MB) dye degradation test. Reprinted with permission from Ref. [116].

#### 4.2. Rare Earth Element Doping

Rare earth elements consist of 15 special lanthanide elements in the Periodic Table of Elements and 2 other elements, Sc and Y, closely related to lanthanide elements. Rare earth elements have abundant energy levels and 4f electron transition characteristics, which can easily form poly-electron configurations to enhance the optical absorption of material and accelerate the efficiency for the separation of photo-generated electron-hole

pairs. Lanthanide-based upconverting GCs contain luminescent fluorides with low phonon energy (i.e., SrF<sub>2</sub>, CaF<sub>2</sub> and NaYF<sub>4</sub>), which can facilitate amplified stimulated emission at low pump power and are highly attractive for upconversion materials or laser applications. The GCs will have a higher refractive index and less photon energy with the addition of the yttrium ion as a nucleation agent [137]. Milewska et al. [138] obtained borate-bismuth GCs containing SrF<sub>2</sub> nanocrystals doped with Eu<sup>3+</sup> ions and found that the luminescence intensity increased after annealing in the samples containing 20 mol% SrF<sub>2</sub>. Through the doping process, some of the Eu<sup>3+</sup> ions were located in the SrF<sub>2</sub> crystalline structure, which would lead to a reduction in the multi-phonon relaxation probability and improvement in the emission efficiency, thereby effectively enhancing the luminescence performance of GCs. Similarly, trivalent erbium ions doped Bi<sub>2</sub>O<sub>3</sub>-B<sub>2</sub>O<sub>3</sub> TGCs containing CaF<sub>2</sub> prepared by Jamalajah et al. [139] showed a significant improvement in the 1.53 μm emission of Er<sup>3+</sup>: 4I<sub>13/2</sub> → 4I<sub>15/2</sub> transition after the formation of Bi<sub>3</sub>B<sub>5</sub>O<sub>12</sub> and CaF<sub>2</sub> in the matrix. The upconversion's emission efficiency in Yb<sup>3+</sup>/Er<sup>3+</sup> co-doped boron bismuth oxyfluoride GCs was greatly enhanced with the precipitation of CaF<sub>2</sub> crystals [140]. In addition, Panyata et al. [141] improved the microstructure of Bi<sub>2</sub>GeO<sub>5</sub> GC by Er<sub>2</sub>O<sub>3</sub> incorporation, making it have a desired crystal dimension.

In recent years, lanthanide-doped photocatalysts have also been extensively studied, continuously absorbing low-energy photons and emitting higher-energy photons, making it possible to use low-energy light, such as near-infrared (NIR) light. The NIR light-responsive upconversion photocatalysts improve the utilization efficiency of sunlight and also have better penetration compared with short-wavelength light and maintain photoactivity, even when the photocatalyst surface is shaded. NIR photocatalysts can be divided into two types: lanthanide direct doping and core-shell structures. Direct doping of lanthanide ions into semiconductors can improve the utilization of light energy and promote the separation efficiency of electron-hole pairs, but the upconversion luminescence efficiency of such NIR photocatalysts is not high enough, which limits its photocatalytic activity [142]. The core-shell structure-type NIR photocatalyst is combined with a light-emitting substrate and a semiconductor, wherein the photoactive center doped with lanthanide ions is the core, and the semiconductor is the surface coating. NIR photocatalysts can capture near-infrared photons and emit upconversion luminescence, which can perform photocatalysis by themselves under NIR light irradiation. Li et al. [122] synthesized a novel core-shell structure (Er<sup>3+</sup>/Yb<sup>3+</sup>-CaO-Al<sub>2</sub>O<sub>3</sub>-SiO<sub>2</sub>-CaF<sub>2</sub>)/TiO<sub>2</sub> NIR photocatalyst by solid-phase reaction for the first time. GC is the host material for upconversion luminescence and the bridge connecting TiO<sub>2</sub>. Compared with pure TiO<sub>2</sub>, the photocatalyst easily collects NIR photons and enhances the photocatalytic activity under NIR and UV-vis-NIR radiation. As shown in Figure 17, based on solid-phase reaction combined with chemical etching, they synthesized BiOCl nanosheets on upconversion SrO-Bi<sub>2</sub>O<sub>3</sub>-B<sub>2</sub>O<sub>3</sub> (SBBO) GC to synthesize NIR PGC [123]. First, rare earth Er<sup>3+</sup>/Yb<sup>3+</sup> doped SrF<sub>2</sub> luminescent nanocrystals were crystallized in SBBO GC particles, and then a new NIR GC photocatalyst coated with BiOCl nanosheets was synthesized by a simple in situ etching method. The PGC also has a core-shell structure, GC powder containing optically active centers Er<sup>3+</sup>, Yb<sup>3+</sup> and Y<sup>3+</sup>-doped SrF<sub>2</sub> nanocrystal, as the core and BiOCl as the surface coating. NIR photocatalysts can efficiently collect NIR photons and emit strong ultraviolet (379 nm), violet (408 nm), green (523 and 540 nm) and red (656 nm) light, which can be used by themselves for photocatalysis. The organic pollutants were degraded under NIR radiation for 90 min, and high removal rates of 66% (norfloxacin) and 79% (methyl orange) were achieved. Meanwhile, they obtained an SBBO upconversion GC that can remove and utilize Cl ions through optimization experiments [124]. Among them, abundant porous structures are continuously formed during the Cl removal process, which further provides channels for the deep migration of Cl<sup>-</sup> and H<sup>+</sup> to its internal Bi source. Under high chloride ion concentration (1300–13,000 mg/L), the Cl<sup>-</sup> removal rate of the best samples all reached more than 96%. The terminal BiOCl-based precipitates are directly collected as NIR photocatalysts with abundant defect heterostructures, excellent upconversion luminescence and electron energy

transport properties. Under UV-Vis–NIR, Vis–NIR and NIR irradiation, the removal rates of norfloxacin (NOR) reached 98%, 73% and 36%, respectively. Similarly, co-worker Zhang et al. [126] also developed a narrow-bandgap  $\text{Bi}_{1.95}\text{Yb}_{0.04}\text{Er}_{0.01}\text{V}_2\text{O}_8$  bulk upconversion PGC by  $\text{Yb}^{3+}/\text{Er}^{3+}$  co-doping. Precipitated crystal  $\text{Bi}_{1.95}\text{Yb}_{0.04}\text{Er}_{0.01}\text{V}_2\text{O}_8$  in volume, this GC also grew  $\text{BiOCl}$  nanosheets in situ on the catalyst surface. The GC produced strong green (526 and 546 nm) and red (658 nm) emissions under 980 nm excitation. Extending the absorption edge of the GC photocatalyst to 620 nm, the NIR photons were efficiently harvested, and most of the upconversion emissions during the photocatalysis process were utilized. A high norfloxacin degradation rate of 55.2% was obtained over 90 min of NIR light irradiation (Figure 18a). Interestingly, the photocatalytic activity of the recycled samples was enhanced again, with the degradation efficiency increased from 48.1% to 55.6% after the HCl etching experiment, which indicated the photocatalyst could be easily regenerated by HCl etching again. Moreover, Figure 18b revealed the photocatalyst could photodegrade low-concentration antibiotics in landfill leachate wastewater, which provided a novel strategy for the practical wastewater treatment. Finally, the photocatalytic mechanism of the photocatalyst is proposed (Figure 18c). The  $\text{BiOCl}$  nanosheet is grown in situ on the surface of the bulk GC, and the lanthanide-doped upconversion luminescence matrices ( $\text{Bi}_{1.95}\text{Yb}_{0.04}\text{Er}_{0.01}\text{V}_2\text{O}_8$ ) crystallized in the GC harvest NIR photons to produce upconversion emissions. The surface coating of  $\text{BiOCl}$  has a wide absorption edge of 620 nm. Direct absorption or fluorescence resonance energy transfer directly uses photons with wavelengths of 652, 792 and  $<620$  nm and excites electrons from the valence band (VB) of  $\text{BiOCl}$  to the conduction band (CB). Then, the electrons of CB  $\text{BiOCl}$  reduce  $\text{O}_2$  to  $\bullet\text{O}_2^-$ , and the holes of VB  $\text{BiOCl}$  oxidize  $\text{OH}^-$  to  $\bullet\text{OH}$ , resulting in the photodegradation of organic pollutants by the active species.

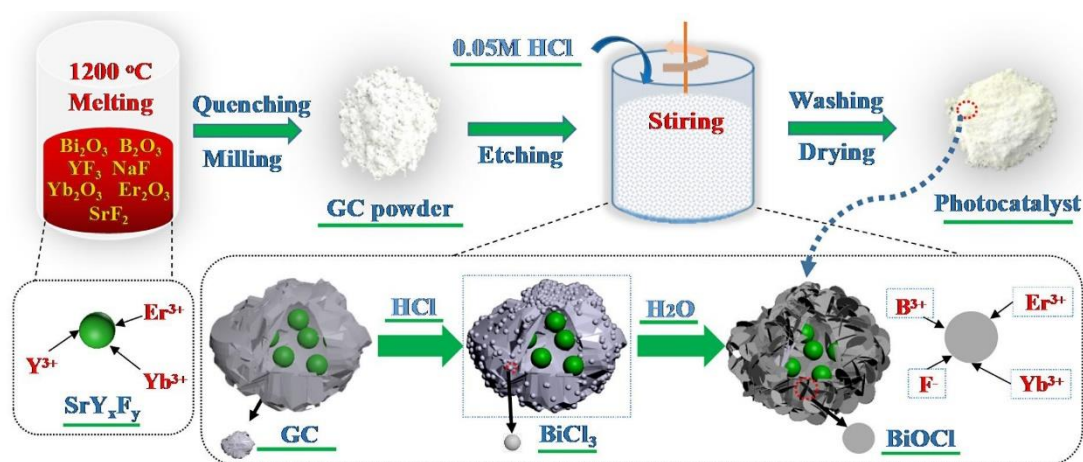


**Figure 17.** Schematic illustration for the preparation of GCs and photocatalyst. Reprinted with permission from Ref. [123].

Compared with conventional binary oxides, perovskite oxides generally exhibit better separation of charge carriers due to higher lattice distortion [143]. Li et al. [127] introduced  $\text{SrTiO}_3$  and  $\text{Sr}_2\text{Bi}_4\text{Ti}_4\text{O}_{15}$  ferroelectric perovskite substrates doped with  $\text{Yb}^{3+}/\text{Er}^{3+}$  rare earth ions in GC and prepared efficient and stable NIR photocatalysts by a facile in situ etching method. The results show exposure of  $\text{Sr}_2\text{Bi}_4\text{Ti}_4\text{O}_{15}$ ,  $\text{SrTiO}_3$  and  $\text{BiOCl}$  in the surface coating of the core-shell structured PGC and constructing a Z-type heterojunction. The heterojunction with built-in electric fields can significantly promote the separation of the charge carrier while trapping the NIR light for photocatalytic reactions. Under NIR illumination for 90 min, the degradation rate of NOR reached 86%, and the PGC can also be used for photodegradation of low-concentration antibiotic-containing wastewater. The  $\text{SrTiO}_3/\text{SrBi}_4\text{Ti}_4\text{O}_{15}@/\text{BiOCl}$  heterojunction was generated during GC formation, which contributed to the generation of  $\bullet\text{O}_2^-$  and  $\bullet\text{OH}$  radicals in the catalytic reaction, which played crucial roles in the degradation process.

However, unlike BiOCl, which has very limited visible light responsive properties, BiOBr exhibits a suitable band gap, good visible-light-driven photocatalytic activity and high chemical stability. Therefore, as shown in Figure 19, Li et al. [125] used the same method to grow BiOBr nanosheets on the surface of SrF<sub>2</sub>-Bi<sub>2</sub>O<sub>3</sub>-B<sub>2</sub>O<sub>3</sub>/Yb<sup>3+</sup>, Tb<sup>3+</sup> (SBBF) on-converted GC. During the in situ etching process, B<sup>3+</sup>, Yb<sup>3+</sup> and Tb<sup>3+</sup> ions in GC can be doped into the BiOBr layer. The lanthanide-doped upconversion luminescence agent (SrF<sub>2</sub>/Yb<sup>3+</sup>, Tb<sup>3+</sup>) in the core of SBBF/ BiOBr-10 harvests NIR photons to then emit red (623 nm), yellow (586 nm), green (546 nm), blue (489 nm), violet (438 and 415 nm) and UV (381 nm) light emissions. The core-shell structured GC@BiOBr heterojunction photocatalyst is beneficial to increase charge transport, reduce the recombination rate of excited carriers and efficiently collect near-infrared photons for UV and visible upconversion emission, which can be utilized in photocatalytic processes. In SBBF/BiOBr-10, the excitation e<sup>-</sup> is promoted to be transferred from the VB to the CB of BiOBr with the energy transfer mechanism, then e<sup>-</sup> is captured by O<sub>2</sub> to produce •O<sub>2</sub><sup>-</sup> free radicals. The PGC showed a high degradation rate of NOR (56%) under NIR illumination for 180 min, and its photocatalytic activity was greatly enhanced under UV-vis-NIR compared with pure BiOBr. Moreover, by re-etching, the photocatalyst can be easily regenerated and made suitable for large-scale fabrication, which will provide a new strategy for the development of efficient photocatalysts.

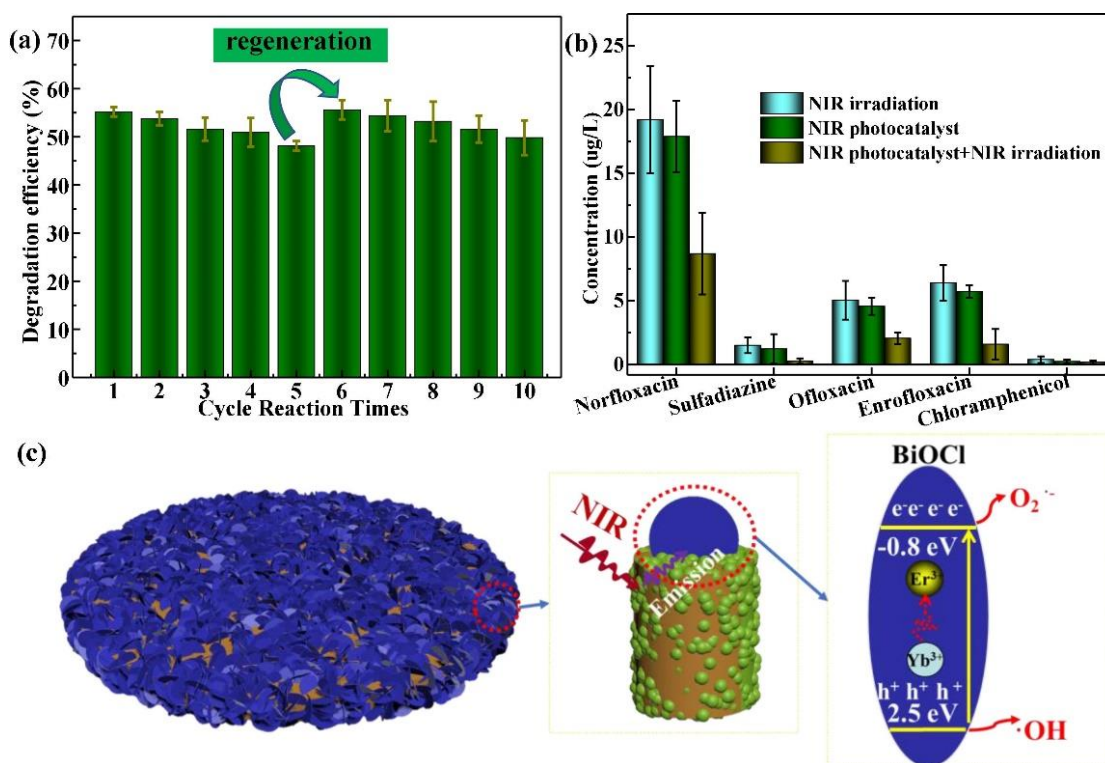


**Figure 18.** (a) Regeneration degradation of Norfloxacin efficiencies under NIR light. (b) Degradation concentration of Norfloxacin, Sulfadiazine, Ofloxacin, Enrofloxacin and Chloramphenicol in concentrated leachate under NIR light. (c) The photocatalytic mechanism of NIR GC photocatalyst. Reprinted with permission from Ref. [126].

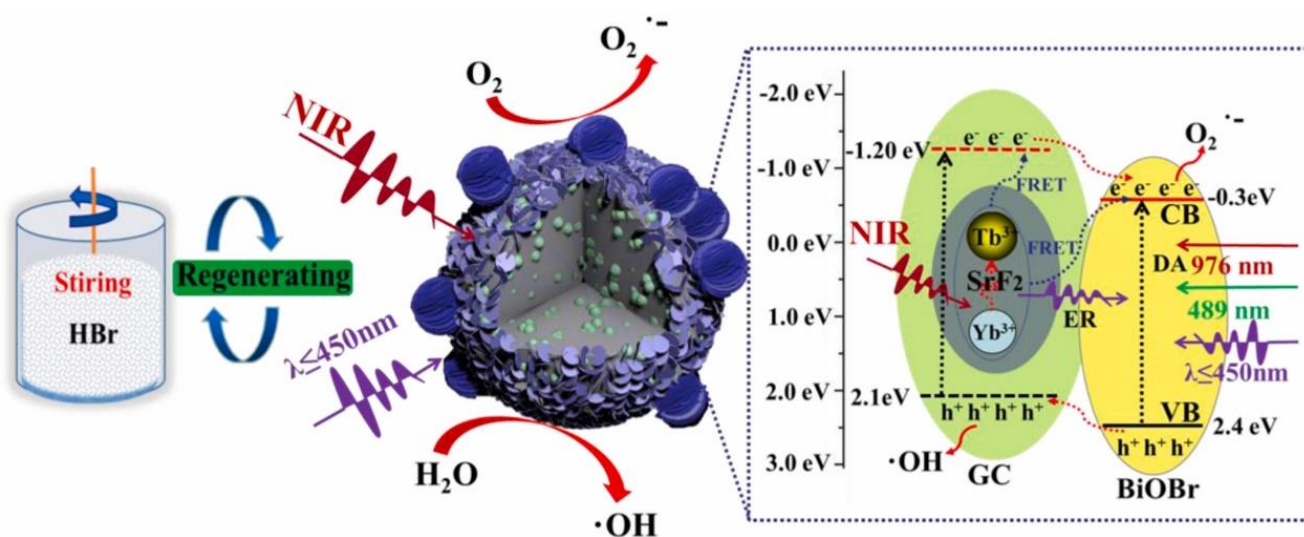


**Figure 19.** Photocatalytic mechanism diagram of SBBF/BiOBr-10. Reprinted with permission from Ref. [125].

#### 4.3. Visible Light Active Photocatalysis

Most photocatalytic materials, including  $\text{TiO}_2$ , only respond to UV light irradiation, with limited functionality and small scale. While it is necessary to develop highly efficient stable visible light active photocatalysts for the purification of large-scale wastewater or air pollution, such as pharmaceutical and chemical wastewater, printing and dyeing textile wastewater, pesticides,  $\text{NO}_x$  and  $\text{SO}_x$ , etc. Consequently, with the goal of maximizing light absorption, maximizing surface charge transfer and minimizing recombination by achieving efficient charge separation and maximizing surface redox reactions, considerable efforts have been devoted to the development of photocatalyst materials with improved performance. Kumar et al. [110] obtained  $\text{TiO}_2$  surface crystallized  $\text{BaO-TiO}_2\text{-B}_2\text{O}_3$  (BTBO) GCs with visible light catalytic activity. Due to the existence of  $\text{TiO}_2$  crystals in crystalline glass, the positive charge on the glass surface has a high electrostatic affinity for negatively charged phosphor-peptides and proteins in the cell membrane, which is conducive to better adhesion to bacterial cells. The antibacterial rate of the crystallized  $\text{BaO-TiO}_2\text{-B}_2\text{O}_3$  glass reached 98.3% under the condition of 2 h of sun irradiation (Figure 20a). Under solar irradiation, electrons move from the valence band to the conduction band of  $\text{TiO}_2$  in the crystalline glass, then excited electrons are generated on the surface of  $\text{TiO}_2$  crystalline glass, triggering a redox reaction (Figure 20c). A redox reaction can produce different reactive oxygen species (ROS) and induce the peroxidation of microbial cells, leading to cell dissolution. ROS produced by hydrolysis enters into cells and increases the oxidative stress inside the cells, thus further enhancing the intracellular ROS production. Intracellular ROS intensity of bacterial cells was almost three times higher in the presence of crystallized glass than in control and as-quenched glass under light (Figure 20d). A Cu-doped  $\text{TeO}_2$ -based GC containing  $\text{TiO}_2$  and  $\text{TiTe}_3\text{O}_8$  visible light active crystals was prepared by Kushwaha et al. [118] using an optimized crystallization method. The visible light photocatalytic activity of the crystallized  $x\text{CaCu}_3\text{Ti}_4\text{O}_{12} - (100-x)\text{TeO}_2$  ( $x = 0.25$  mol% to 3 mol%) glass was investigated for estrogenic pharmaceutical pollutants, and the degradation rate was observed as  $168.56 \text{ min}^{-1} \cdot \text{m}^{-2}$  ( $x = 3 \text{ mol}\%$ ). This crystallized glass plate also behaved at a higher visible light photocatalytic  $\text{H}_2$  production rate ( $135 \mu\text{mol h}^{-1} \text{ g}^{-1}$ ). The catalytic efficiency of this visible light-driven multifunctional photocatalyst depends on the active concentration of the photoactive crystallites present in the glass matrix. Iida et al. [119] added  $\text{Al}_2\text{O}_3$  to iron-containing soda lime silicate glass to obtain  $15\text{Na}_2\text{O} \cdot 15\text{CaO} \cdot 40\text{Fe}_2\text{O}_3 \cdot x\text{Al}_2\text{O}_3 \cdot (30-x)\text{SiO}_2$  glass ( $x\text{NCFAS}$ ). With the increase in alumina content, the content of  $\alpha\text{-Fe}_2\text{O}_3$  decreased and the content of  $\text{Ca}_2\text{Fe}_{22}\text{O}_{33}$  or  $\text{CaFe}_2\text{O}_4$  increased. The introduction of alumina enhanced the photocatalytic degradation activity

of iron-containing soda lime silicate glass for methylene blue (MB). It is concluded that the precipitation amount of  $\alpha$ - $\text{Fe}_2\text{O}_3$  and the high light transmittance caused by the introduction of  $\text{Al}_2\text{O}_3$  are essential for the visible light photocatalytic activity of xNCFAS glass. For the first time, Margha et al. [120] combined the highly photoactive metastable  $\beta$ - and  $\gamma$ - $\text{Bi}_2\text{O}_3$  phases with  $\text{BiFeO}_3$  in one GC material. The best photocatalytic performance for the degradation of the RY160 dye was exhibited with the sample containing equal amounts of  $\text{Fe}_2\text{O}_3$  and  $\text{Bi}_2\text{O}_3$  due to the formation of a  $\gamma$ - $\text{Bi}_2\text{O}_3/\text{BiFeO}_3$  heterojunction. As shown in Figure 21a, Kadam et al. [121] proposed a novel approach to generate bismuth sulfide ( $\text{Bi}_2\text{S}_3$ ) QDs in silicate glass. The photocatalytic hydrogen ( $\text{H}_2$ ) production under solar light was performed and the maximum  $\text{H}_2$  generation, i.e.,  $6418.8 \text{ mmol h}^{-1} \text{ g}^{-1}$ , was achieved for the sample containing 7 mg  $\text{Bi}_2\text{S}_3$  quantum dots (Figure 21b). It is noteworthy that the enhanced  $\text{H}_2$  evolution rate has been obtained for glass nanocomposites having increased concentration and density of  $\text{Bi}_2\text{S}_3$  QDs. Another beauty of this photocatalytic material is that it can be reused several times without a reduction in its activity. To achieve visible light-driven photocatalysis, common methods investigated for performance improvement are morphology optimization, doping, using sensitizers and/or co-catalysts and using different types of heterojunctions [144]. However, the improvement in visible light-active PGCs still lacks systematic exploration.

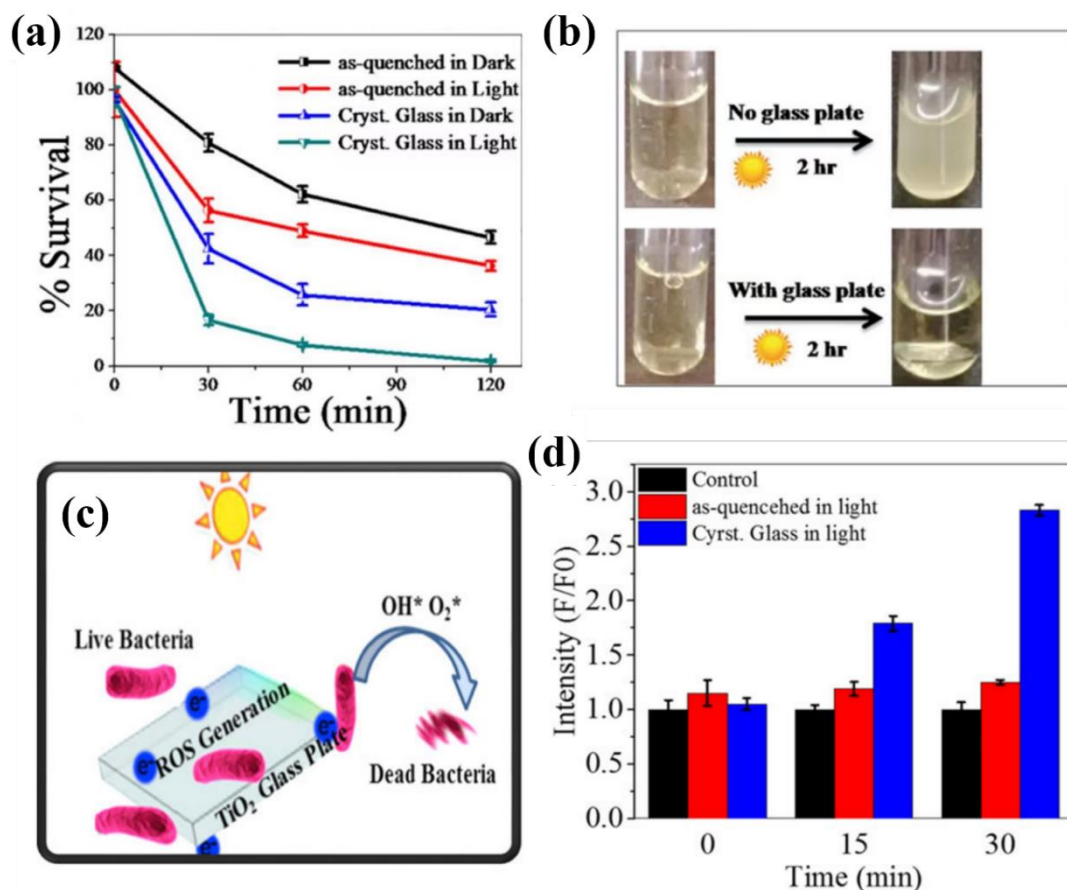


**Figure 20.** (a) % survival of *E. coli* in dark and under light irradiation from dilution plate method. (b) Typical image of *E. coli* suspension of bacteria in test tubes with and without crystallized glass under 2 h sunlight exposure and then after 24 h incubation. (c) Schematic of proposed antibacterial mechanism under solar irradiation. (d) Intracellular ROS measurement of bacterial cells in control, as-quenched and crystallized experimental group by relative DCFH fluorescence intensity. Reprinted with permission from Ref. [110].

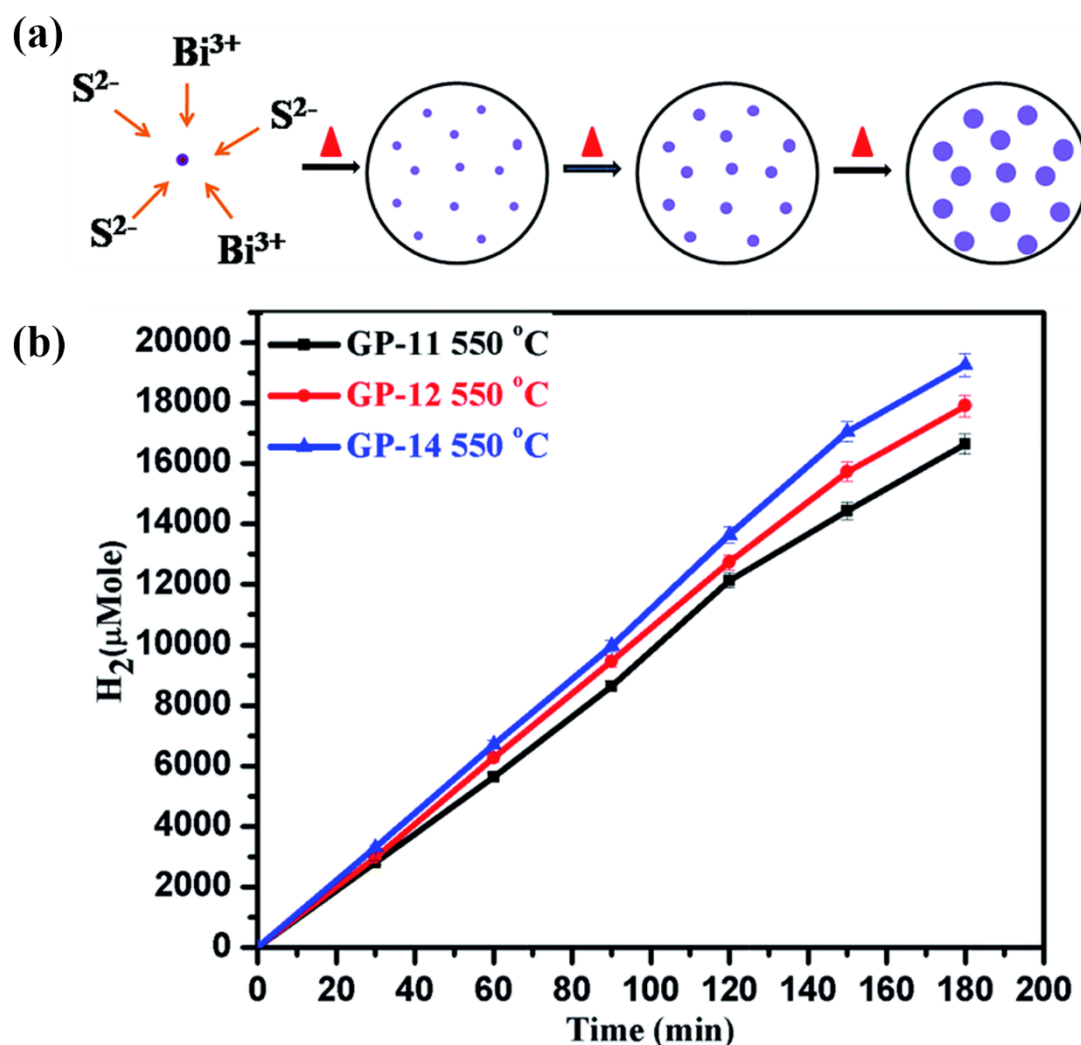


**Figure 21.** (a) Schematic diagram of the formation and growth mechanism of  $\text{Bi}_2\text{S}_3$  QDs in a glass matrix. (b) Photocatalytic activities of glass composites GP-11, GP-12 and GP-14 obtained by heat treatment at  $550^\circ\text{C}$  for 8 h. Reprinted with permission from Ref. [121].

This section elaborates the modification strategies of PGCs to improve their photocatalytic activity by chemical etching and rare earth doping, as well as the requirements for visible light photocatalytic materials (Figure 22). Chemical etching makes the glass surface form a network porous hierarchy, which is conducive to better capture light, leading to more efficient photocatalysis. Moreover, the increase in roughness caused by etching is more conducive to the adsorption of pollutants, and the decrease in grain size is conducive to transparency, while the increase in transparency will lead to the activation of more photocatalytic crystals. Doping rare earth elements greatly improves the upconversion emission efficiency of GCs. Through the energy conversion mechanism of direct absorption (DA), emission reabsorption (ER) and Förster resonance energy transfer (FRET), a photocatalysis response is generated in near-infrared. NIR light has a higher penetration depth through various media, especially biological tissues and wastewater. Under UV-vis–NIR light irradiation, the NIR driven degradation of organic pollutants can be achieved, and the photocatalytic efficiency under UV-vis–NIR light irradiation can be improved. At the same time, rare earth elements doped into the lattice will lead to the contraction and reduction in the crystal size. At present, there are few GCs that can realize visible light photocatalysis, which is very demanding for the crystallinity and transparency of GCs, requiring a higher concentration of visible light-active microcrystals to precipitate from the glass matrix. Photocatalytic microcrystals absorb light to the maximum extent so as to

improve effective charge separation efficiency and maximize surface redox reaction, thus maximizing the photocatalytic efficiency of PGCs for various application fields.

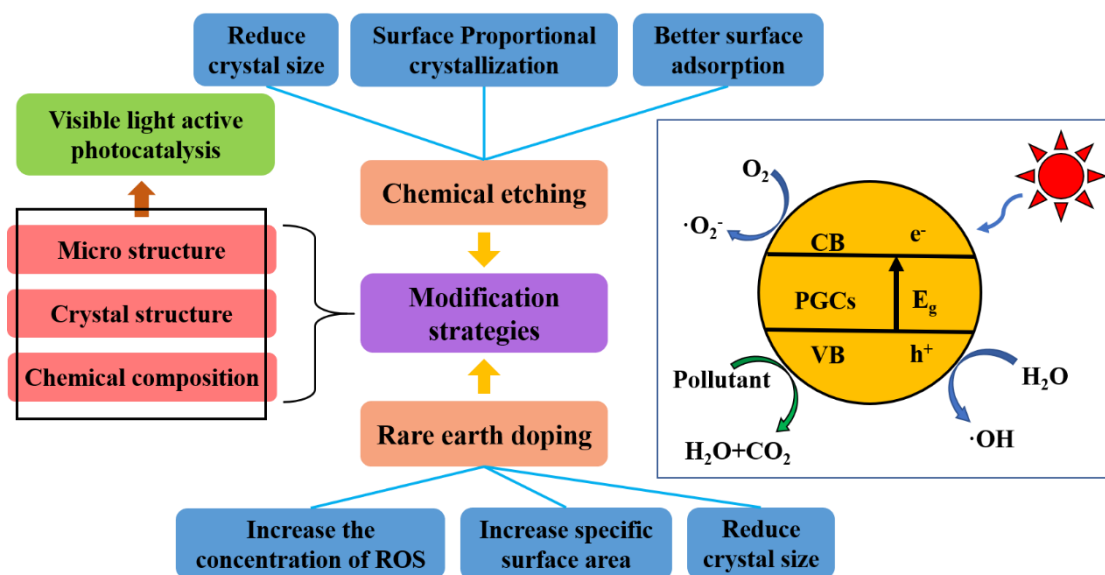


Figure 22. Summary of modification engineering for PGCs.

## 5. Conclusions and Future Prospects

### 5.1. Conclusions

In conclusion, this review highlights the basic theories, design strategies, crystallization methods and modification investigations of GC photocatalysts. Obviously, GCs have proven to be one of the candidate materials suitable for designing and fabricating advanced photocatalysts for various applications. PGCs have the following advantages: (i) photocatalytic crystals embedded in the matrix without any leaching problems, (ii) easy to manufacture in different shapes and sizes for applications and (iii) high transparency to maximize photocatalytic activity. PGCs have broad application prospects in water purification, bacterial disinfection, self-cleaning and hydrogen evolution. Whether it is surface crystallization, bulk crystallization or a combination of the two, GCs with desired properties can be designed by controlling crystallization. Maintaining high transparency enables the activation of photocatalytic crystals on the inner-surface of TGCs during the photocatalytic process, resulting in highly efficient photocatalytic performance. Transparency can be achieved by controlling glass composition and crystal size, rate crystallization, crystal distribution, and the like. In particular, the transparency of TGCs by congruent crystallization with almost identical composition of crystalline and glass matrix is appreciable. Similar to the wet chemical process, different types of crystals can be precipitated into the glassy phase by different processes. Among solid-phase glasses, direct reaction of the solvent phase is the most popular approach for synthesizing NCs in glasses. Furthermore, different strategies to enhance their photocatalytic activity, including chemical etching, rare earth metals doping, non-metallic or metal dopants, etc., have also been proposed. These modification methods are conducive to improving the microstructure, the size of crystal, so as to obtain more efficient photocatalysis.

### 5.2. Future Prospects

Up to now, although research on GCs has made preliminary progress in recent years, there are still several challenges in rationally preparing efficient PGCs that are suitable for various applications, controlling the transparency and surface crystallization of GCs and improving the photocatalytic activity under visible light. Due to the refractive index difference between nanocrystals and the glass matrix and the Mie scattering effect caused by oversized grains, it is difficult to obtain high transparency in most GCs. Studies have

shown that PGCs with high photocatalytic activity required high crystallinity. However, the higher crystallinity is bound to significantly reduce the transparency and even cause defects that reduce the photocatalytic efficiency. Therefore, there is a long way to go in balancing transparency and crystallinity (photocatalytic activity) in the preparation and application of PGCs.

Furthermore, although conventional GCs have received extensive attention due to their natural advantages, such as low cost, ease of manufacture, transparency, chemical and mechanical stability, the chemical stability and recyclability of PGC materials have a large gap to real time application in fields of energy conversion and environmental remediation because of different applied conditions. It has been shown that the feasibility of precipitation or fixation of photocatalyst nanocrystals in GCs to avoid disadvantages of photocatalytic nanocrystals applied in form of powder and film, such as difficulty in recovery of nanopowder, secondary pollution, low adhesion between photocatalytic coating and substrate material, short service life and less recyclability, is limited. However, these PGC materials are usually assessed using only model organic contaminants. How PGC materials perform (stability, recyclability, efficiency, etc.) in the real case of decontamination, especially in extreme conditions, has not been explored systematically. Furthermore, it is well known that some parent glass systems for preparing PGC such as borate, phosphate and tellurite glass systems, have relatively weak chemical durability due to their hygroscopic properties; thereby, it is vitally important for real time application to choose suitable parent glass system and photocatalytic active crystals.

Additionally, the function of currently reported PGCs is relatively simple; investigation and exploration on the multifunctional PGCs with high photocatalytic performance, the broad photocatalytic response from UV and visible to near infrared (NIR) ranges, and high transparency is of great significance. The crystalline grains (quantum dots, nanoparticles containing rare earth ions such as Yb, Nd, Tm, Er, Ho, Pr, etc.) with light conversion luminescence and the grains (Ti, Zn, Bi and other compounds) with photocatalytic function need to be precipitated simultaneously in GCs. Co-precipitation of light conversion luminescent crystals into PGC can improve the optical response range of PGC and energy transfer between luminescent grains and photocatalytic active grains, thus increasing the photocatalytic performance of PGC materials. Thereby, precipitation of crystallites in PGCs to broaden the range of light absorption to the NIR region and convert to UV and visible emission is desirable. The visible light and near-infrared light can be fully utilized efficiently for photocatalysis by up-conversion of near-infrared light. At the same time, to ensure the effective activation of photocatalytic grains precipitated on the surface of PGCs by incident sunlight and upconversion luminescence, designing the spatial distribution and controlling the nucleation and growth process of conversion luminescence grains and photocatalytic grains can solve the problem of translucence and even opacity of PGCs caused by crystallization. Finally, PGC materials with highly efficient antibacterial, disinfectant activities and air cleaning properties indoors will be strongly focused on, as COVID-19 and another infectious virus are spreading across the world. These surveys remain in their infancy, and there are still numerous research gaps worth exploring in the near future.

**Funding:** This work was supported by the National Natural Science Foundation of China (51974168), Science and Technology Major Project of Inner Mongolia Autonomous Region in China (2019ZD023 and 2021ZD0028) and State Key Laboratory of Silicate Materials for Architectures (Wuhan University of Technology) (SYSJJ2020-08).

**Conflicts of Interest:** The authors declare no conflict of interest.

## References

1. Kumar, S.G.; Devi, L.G. Review on modified TiO<sub>2</sub> photocatalysis under UV/visible light: Selected results and related mechanisms on interfacial charge carrier transfer dynamics. *J. Phys. Chem. A* **2011**, *115*, 13211–13241. [[CrossRef](#)]
2. Kabra, K.; Chaudhary, R.; Sawhney, R.L. Treatment of Hazardous Organic and Inorganic Compounds. *Ind. Eng. Chem. Res.* **2004**, *43*, 7683–7696. [[CrossRef](#)]

3. McCullagh, C.; Robertson, J.M.C.; Bahnemann, D.W.; Robertson, P.K.J. The application of TiO<sub>2</sub> photocatalysis for disinfection of water contaminated with pathogenic micro-organisms: A review. *Res. Chem. Intermed.* **2007**, *33*, 359–375. [[CrossRef](#)]
4. Fujishima, A.; Honda, K. Electrochemical photolysis of water at a semiconductor electrode. *Nature* **1972**, *238*, 37–38. [[CrossRef](#)] [[PubMed](#)]
5. Schneider, J.; Matsuoka, M.; Takeuchi, M.; Zhang, J.; Horiuchi, Y.; Anpo, M.; Bahnemann, D.W. Understanding TiO<sub>2</sub> photocatalysis: Mechanisms and materials. *Chem. Rev.* **2014**, *114*, 9919–9986. [[CrossRef](#)] [[PubMed](#)]
6. Zhang, H.; Zong, R.; Zhao, J.; Zhu, Y. Dramatic Visible Photocatalytic Degradation Performances Due to Synergetic Effect of TiO<sub>2</sub> with PANI. *Environ. Sci. Technol.* **2008**, *42*, 3803–3807. [[CrossRef](#)] [[PubMed](#)]
7. Fu, J. Photocatalytic properties of glass ceramics containing anatase-type TiO<sub>2</sub>. *Mater. Lett.* **2012**, *68*, 419–422. [[CrossRef](#)]
8. Fu, G.; Vary, P.S.; Lin, C.-T. Anatase TiO<sub>2</sub> Nanocomposites for Antimicrobial Coatings. *J. Phys. Chem. B* **2005**, *109*, 8889–8898. [[CrossRef](#)] [[PubMed](#)]
9. Linsebigler, A.L.; Lu, G.; John, T.; Yates, J. Photocatalysis on TiO<sub>2</sub> Surfaces: Principles, Mechanisms, and Selected Results. *Chem. Rev.* **1995**, *95*, 735–758. [[CrossRef](#)]
10. Huang, H.; Li, X.; Wang, J.; Dong, F.; Chu, P.K.; Zhang, T.; Zhang, Y. Anionic Group Self-Doping as a Promising Strategy: Band-Gap Engineering and Multi-Functional Applications of High-Performance CO<sub>3</sub><sup>2-</sup>-Doped Bi<sub>2</sub>O<sub>2</sub>CO<sub>3</sub>. *ACS Catal.* **2015**, *5*, 4094–4103. [[CrossRef](#)]
11. Huang, H.; He, Y.; Li, X.; Li, M.; Zeng, C.; Dong, F.; Du, X.; Zhang, T.; Zhang, Y. Bi<sub>2</sub>O<sub>2</sub>(OH)(NO<sub>3</sub>) as a desirable [Bi<sub>2</sub>O<sub>2</sub>]<sup>2+</sup> layered photocatalyst: Strong intrinsic polarity, rational band structure and {001} active facets co-beneficial for robust photooxidation capability. *J. Mater. Chem. A* **2015**, *3*, 24547–24556. [[CrossRef](#)]
12. Huang, H.; Xiao, K.; He, Y.; Zhang, T.; Dong, F.; Du, X.; Zhang, Y. In situ assembly of BiOI@Bi<sub>12</sub>O<sub>17</sub>Cl<sub>2</sub> p-n junction: Charge induced unique front-lateral surfaces coupling heterostructure with high exposure of BiOI {001} active facets for robust and nonselective photocatalysis. *Appl. Catal. B Environ.* **2016**, *199*, 75–86. [[CrossRef](#)]
13. Huang, H.; He, Y.; Lin, Z.; Kang, L.; Zhang, Y. Two Novel Bi-Based Borate Photocatalysts: Crystal Structure, Electronic Structure, Photoelectrochemical Properties, and Photocatalytic Activity under Simulated Solar Light Irradiation. *J. Phys. Chem. C* **2013**, *117*, 22986–22994. [[CrossRef](#)]
14. Hama Aziz, K.H. Application of different advanced oxidation processes for the removal of chloroacetic acids using a planar falling film reactor. *Chemosphere* **2019**, *228*, 377–383. [[CrossRef](#)] [[PubMed](#)]
15. Hama Aziz, K.H.; Omer, K.M.; Mahyar, A.; Miessner, H.; Mueller, S.; Moeller, D. Application of Photocatalytic Falling Film Reactor to Elucidate the Degradation Pathways of Pharmaceutical Diclofenac and Ibuprofen in Aqueous Solutions. *Coatings* **2019**, *9*, 465. [[CrossRef](#)]
16. Romero, M.; Rincon, J.S.M. Surface and Bulk Crystallization of Glass-Ceramic in the Na<sub>2</sub>O-CaO-ZnO-PbO-Fe<sub>2</sub>O<sub>3</sub>-Al<sub>2</sub>O<sub>3</sub>-SiO<sub>2</sub> System Derived from a Goethite Waste. *J. Am. Ceram. Soc.* **1999**, *82*, 1313–1317. [[CrossRef](#)]
17. Brow, R.K.; Schmitt, M.L. A survey of energy and environmental applications of glass. *J. Eur. Ceram. Soc.* **2009**, *29*, 1193–1201. [[CrossRef](#)]
18. Lebullenger, R.; Chenu, S.; Rocherullé, J.; Merdrignac-Conanec, O.; Cheviré, F.; Tessier, F.; Bouzaza, A.; Brosillon, S. Glass foams for environmental applications. *J. Non-Cryst. Solids* **2010**, *356*, 2562–2568. [[CrossRef](#)]
19. Beall, G.H. Design and Properties of Glass-Ceramics. *Annu. Rev. Mater. Sci.* **1992**, *22*, 91–119. [[CrossRef](#)]
20. Karpukhina, N.; Hill, R.G.; Law, R.V. Crystallisation in oxide glasses—A tutorial review. *Chem. Soc. Rev.* **2014**, *43*, 2174–2186. [[CrossRef](#)]
21. Righini, G.C.; Pablos-Martin, A.D.; Pascual, M.J.; Ferrari, M. Glass-Ceramics: A Class of Nanostructured Materials for Photonics. *La Riv. Del Nuovo Cim.* **2015**, *38*, 311–369.
22. Höland, W.; Beall, G.H. Chapter 3: Microstructure Control. In *Glass-Ceramic Technology*, 2nd ed.; John Wiley & Sons: Hoboken, NJ, USA, 2012.
23. Komatsu, T. Design and control of crystallization in oxide glasses. *J. Non-Cryst. Solids* **2015**, *428*, 156–175. [[CrossRef](#)]
24. Zanutto, E.D. A bright future for glass-ceramics. *Am. Ceram. Soc. Bull.* **2010**, *89*, 19–27.
25. Montazerian, M.; Singh, S.P.; Zanutto, E.D. An analysis of glass-ceramic research and commercialization. *Am. Ceram. Soc. Bull.* **2015**, *94*, 30–35.
26. Stookey, S.D. Catalyzed Crystallization of Glass in Theory and Practice. *Ind. Eng. Chem.* **1959**, *51*, 805–808. [[CrossRef](#)]
27. Sakamoto, A.; Yamamoto, S. Glass-Ceramics: Engineering Principles and Applications. *Int. J. Appl. Glass Sci.* **2010**, *1*, 237–247. [[CrossRef](#)]
28. Beall, G.H.; Pinckney, L.R. Nanophase Glass-Ceramics. *J. Am. Ceram. Soc.* **2009**, *82*, 5–16. [[CrossRef](#)]
29. Liu, X.; Zhou, J.; Zhou, S.; Yue, Y.; Qiu, J. Transparent glass-ceramics functionalized by dispersed crystals. *Prog. Mater. Sci.* **2018**, *97*, 38–96. [[CrossRef](#)]
30. Casasola, R.; Rincón, J.M.; Romero, M. Glass-ceramic glazes for ceramic tiles: A review. *J. Mater. Sci.* **2011**, *47*, 553–582. [[CrossRef](#)]
31. Pinckney, L.R.; Beall, G.H. Microstructural Evolution in Some Silicate Glass-Ceramics: A Review. *J. Am. Ceram. Soc.* **2008**, *91*, 773–779. [[CrossRef](#)]
32. Wenderich, K.; Mul, G. Methods, Mechanism, and Applications of Photodeposition in Photocatalysis: A Review. *Chem. Rev.* **2016**, *116*, 14587–14619. [[PubMed](#)]
33. Singh, G.; Sharma, M.; Vaish, R. Emerging trends in glass-ceramic photocatalysts. *Chem. Eng. J.* **2021**, *407*, 126971. [[CrossRef](#)]

34. Teh, C.M.; Mohamed, A.R. Roles of titanium dioxide and ion-doped titanium dioxide on photocatalytic degradation of organic pollutants (phenolic compounds and dyes) in aqueous solutions: A review. *J. Alloys Compd.* **2011**, *509*, 1648–1660. [[CrossRef](#)]
35. Li Puma, G.; Bono, A.; Krishnaiah, D.; Collin, J.G. Preparation of titanium dioxide photocatalyst loaded onto activated carbon support using chemical vapor deposition: A review paper. *J. Hazard. Mater.* **2008**, *157*, 209–219. [[CrossRef](#)]
36. Srikanth, B.; Goutham, R.; Badri Narayan, R.; Ramprasath, A.; Gopinath, K.P.; Sankaranarayanan, A.R. Recent advancements in supporting materials for immobilised photocatalytic applications in waste water treatment. *J. Environ. Manag.* **2017**, *200*, 60–78. [[CrossRef](#)]
37. Li, X.; Yu, J.; Low, J.; Fang, Y.; Xiao, J.; Chen, X. Engineering heterogeneous semiconductors for solar water splitting. *J. Mater. Chem. A* **2015**, *3*, 2485–2534.
38. Wen, J.; Xie, J.; Chen, X.; Li, X. A review on g-C<sub>3</sub>N<sub>4</sub>-based photocatalysts. *Appl. Surf. Sci.* **2017**, *391*, 72–123. [[CrossRef](#)]
39. Zanotto, E.D.; Tsuchida, J.E.; Schneider, J.F.; Eckert, H. Thirty-year quest for structure–nucleation relationships in oxide glasses. *Int. Mater. Rev.* **2015**, *60*, 376–391. [[CrossRef](#)]
40. Zanotto, E.D. Glass Crystallization Research—A 36-Year Retrospective. Part I, Fundamental Studies. *Int. J. Appl. Glass Sci.* **2013**, *4*, 105–116. [[CrossRef](#)]
41. Schmelzer, J.; Möller, J.; Gutzow, I. Ostwald’s Rule of Stages: The Effect of Elastic Strains and External Pressure. *Z. Für Phys. Chem.* **1998**, *204*, 171–181. [[CrossRef](#)]
42. Zanotto, E.D.; Müller, E. A simple method to predict the nucleation mechanism in glass. *J. Non-Cryst. Solids* **1991**, *130*, 220–221. [[CrossRef](#)]
43. Yazawa, T.; Machida, F.; Oki, K.; Mineshige, A.; Kobune, M. Novel porous TiO<sub>2</sub> glass-ceramics with highly photocatalytic ability. *Ceram. Int.* **2009**, *35*, 1693–1697. [[CrossRef](#)]
44. Singh, G.; Kumar, S.; Sharma, S.K.; Sharma, M.; Singh, V.P.; Vaish, R. Antibacterial and photocatalytic active transparent TiO<sub>2</sub> crystallized CaO–BaO–B<sub>2</sub>O<sub>3</sub>–Al<sub>2</sub>O<sub>3</sub>–TiO<sub>2</sub>–ZnO glass nanocomposites. *J. Am. Ceram. Soc.* **2019**, *102*, 3378–3390. [[CrossRef](#)]
45. Fu, J. Photocatalytic properties of TiO<sub>2</sub>–P<sub>2</sub>O<sub>5</sub> glass ceramics. *Mater. Res. Bull.* **2011**, *46*, 2523–2526. [[CrossRef](#)]
46. Fu, J. Highly photocatalytic glass ceramics containing MgTi<sub>4</sub>(PO<sub>4</sub>)<sub>6</sub> crystals. *Mater. Lett.* **2014**, *118*, 84–87. [[CrossRef](#)]
47. Margha, F.H.; Badawy, M.I.; Gad-Allah, T.A. ZnO enriched transparent glass-ceramics for wastewater decontamination. *Environ. Prog. Sustain. Energy* **2017**, *36*, 442–447. [[CrossRef](#)]
48. Singh, G.; Kumar, S.; Singh, V.P.; Vaish, R. Transparent ZnO crystallized glass ceramics for photocatalytic and antibacterial applications. *J. Appl. Phys.* **2019**, *125*, 175102. [[CrossRef](#)]
49. Almeida, E.F.D.; Paiva, J.a.C.D.; Sombra, A.S.B. Infrared and complex dielectric function studies of LiNbO<sub>3</sub> in niobate glass-ceramics. *J. Mater. Sci.* **2000**, *35*, 1555–1559. [[CrossRef](#)]
50. Senthil Murugan, G.; Varma, K.B.R.; Takahashi, Y.; Komatsu, T. Nonlinear-optic and ferroelectric behavior of lithium borate–strontium bismuth tantalate glass–ceramic composite. *Appl. Phys. Lett.* **2001**, *78*, 4019–4021. [[CrossRef](#)]
51. Marghussian, V.K. *Nano-Glass Ceramics: Processing, Properties and Applications*; Elsevier: Oxford, UK; Waltham, MA, USA, 2015.
52. Kerker, K. *The Scattering of Light*; Academic Press: New York, NY, USA, 1969.
53. Andreev, N.S. Scattering of visible light by glasses undergoing phase separation and homogenization. *J. Non-Cryst. Solids* **1978**, *30*, 99–126. [[CrossRef](#)]
54. Hopper, R.W. Stochastic theory of scattering from idealized spinodal structures: II. Scattering in general and for the basic late stage model. *J. Non-Cryst. Solids* **1985**, *70*, 111–142. [[CrossRef](#)]
55. Syam Prasad, N.; Varma, K.B.R.; Takahashi, Y.; Benino, Y.; Fujiwara, T.; Komatsu, T. Evolution and characterization of fluorite-like nano-SrBi<sub>2</sub>Nb<sub>2</sub>O<sub>9</sub> phase in the SrO–Bi<sub>2</sub>O<sub>3</sub>–Nb<sub>2</sub>O<sub>5</sub>–Li<sub>2</sub>B<sub>4</sub>O<sub>7</sub> glass system. *J. Solid State Chem.* **2003**, *173*, 209–215. [[CrossRef](#)]
56. Molla, A.R.; Tarafder, A.; Karmakar, B. Synthesis and properties of glasses in the K<sub>2</sub>O–SiO<sub>2</sub>–Bi<sub>2</sub>O<sub>3</sub>–TiO<sub>2</sub> system and bismuth titanate (Bi<sub>4</sub>Ti<sub>3</sub>O<sub>12</sub>) nano glass–ceramics thereof. *J. Mater. Sci.* **2010**, *46*, 2967–2976. [[CrossRef](#)]
57. Lin, G.; Luo, F.; Pan, H.; Smedskjaer, M.M.; Teng, Y.; Chen, D.; Qiu, J.; Zhao, Q. Universal Preparation of Novel Metal and Semiconductor Nanoparticle–Glass Composites with Excellent Nonlinear Optical Properties. *J. Phys. Chem. C* **2011**, *115*, 24598–24604. [[CrossRef](#)]
58. Singh, S.P.; Karmakar, B. Oxidative control of surface plasmon resonance of bismuth nanometal in bismuth glass nanocomposites. *Mater. Chem. Phys.* **2010**, *119*, 355–358. [[CrossRef](#)]
59. Masai, H.; Fujiwara, T.; Mori, H.; Komatsu, T. Fabrication of TiO<sub>2</sub> nanocrystallized glass. *Appl. Phys. Lett.* **2007**, *90*, 081907. [[CrossRef](#)]
60. Haily, E.; Bih, L.; El Bouari, A.; Lahmar, A.; El Marssi, M.; Manoun, B. Structural, optical, and dielectric properties of Bi<sub>2</sub>O<sub>3</sub>–K<sub>2</sub>O–TiO<sub>2</sub>–P<sub>2</sub>O<sub>5</sub> glasses and related glass-ceramics. *Phase Transit.* **2020**, *93*, 1030–1047. [[CrossRef](#)]
61. Holand, W.; Beall, G.H. Chapter 2: Composition Systems for Glass–Ceramics. In *Glass Ceramic Technology*; John Wiley & Sons: Hoboken, NJ, USA, 2012.
62. Sharma, S.K.; Singh, V.P.; Chauhan, V.S.; Kushwaha, H.S.; Vaish, R. Photocatalytic self-cleaning transparent 2Bi<sub>2</sub>O<sub>3</sub>–B<sub>2</sub>O<sub>3</sub> glass ceramics. *J. Appl. Phys.* **2017**, *122*, 094901. [[CrossRef](#)]
63. Singh, V.P.; Kushwaha, H.S.; Vaish, R. Photocatalytic study on SrBi<sub>2</sub>B<sub>2</sub>O<sub>7</sub> (SrO–Bi<sub>2</sub>O<sub>3</sub>–B<sub>2</sub>O<sub>3</sub>) transparent glass ceramics. *Materials Res. Bull.* **2018**, *99*, 453–459. [[CrossRef](#)]

64. Bertrand, A.; Carreaud, J.; Delaizir, G.; Shimoda, M.; Duclère, J.-R.; Colas, M.; Belleil, M.; Cornette, J.; Hayakawa, T.; Genevois, C.; et al. New Transparent Glass-Ceramics Based on the Crystallization of “Anti-glass” Spherulites in the  $\text{Bi}_2\text{O}_3\text{-Nb}_2\text{O}_5\text{-TeO}_2$  System. *Cryst. Growth Des.* **2015**, *15*, 5086–5096. [[CrossRef](#)]
65. Deubener, J.; Allix, M.; Davis, M.J.; Duran, A.; Höche, T.; Honma, T.; Komatsu, T.; Krüger, S.; Mitra, I.; Müller, R.; et al. Updated definition of glass-ceramics. *J. Non-Cryst. Solids* **2018**, *501*, 3–10. [[CrossRef](#)]
66. Margha, F.H.; Abdel-Wahed, M.S.; Gad-Allah, T.A. Nanocrystalline  $\text{Bi}_2\text{O}_3\text{-B}_2\text{O}_3\text{-}(\text{MoO}_3 \text{ or } \text{V}_2\text{O}_5)$  glass-ceramic systems for organic pollutants degradation. *Ceram. Int.* **2015**, *41*, 5670–5676. [[CrossRef](#)]
67. Lee, Y.K.; Lee, J.S.; Heo, J.; Im, W.B.; Chung, W.J. Phosphor in glasses with Pb-free silicate glass powders as robust color-converting materials for white LED applications. *Opt. Lett.* **2012**, *37*, 3276–3278. [[CrossRef](#)] [[PubMed](#)]
68. Luo, Z.; Liu, W.; Qu, G.; Lu, A.; Han, G. Sintering behavior, microstructure and mechanical properties of various fluorine-containing Y-SiAlON glass-ceramics. *J. Non-Cryst. Solids* **2014**, *388*, 62–67. [[CrossRef](#)]
69. Sainz, M.A.; Miranzo, P.; Osendi, M.I. Sintering behaviour and properties of YAlSiO and YAlSiON glass-ceramics. *Ceram. Int.* **2011**, *37*, 1485–1492. [[CrossRef](#)]
70. Gajc, M.; Surma, H.B.; Klos, A.; Sadecka, K.; Orlinski, K.; Nikolaenko, A.E.; Zdunek, K.; Pawlak, D.A. Nanoparticle Direct Doping: Novel Method for Manufacturing Three-Dimensional Bulk Plasmonic Nanocomposites. *Adv. Funct. Mater.* **2013**, *23*, 3443–3451. [[CrossRef](#)]
71. Karaksina, E.V.; Shiryayev, V.S.; Ketkova, L.A. Preparation of composite materials for fiber optics based on chalcogenide glasses containing ZnS (ZnSe): Cr (2+) crystals. *J. Non-Cryst. Solids* **2013**, *377*, 220–224. [[CrossRef](#)]
72. Zhou, Y.; Chen, D.; Tian, W.; Ji, Z.; Hintzen, H.T.J.M. Impact of  $\text{Eu}^{3+}$  Dopants on Optical Spectroscopy of  $\text{Ce}^{3+}$ :  $\text{Y}_3\text{Al}_5\text{O}_{12}$ -Embedded Transparent Glass-Ceramics. *J. Am. Ceram. Soc.* **2015**, *98*, 2445–2450. [[CrossRef](#)]
73. Huang, J.; Hu, X.; Shen, J.; Wu, D.; Yin, C.; Xiang, R.; Yang, C.; Liang, X.; Xiang, W. Facile synthesis of a thermally stable  $\text{Ce}^{3+}$ :  $\text{Y}_3\text{Al}_5\text{O}_{12}$  phosphor-in-glass for white LEDs. *Cryst. Eng. Comm.* **2015**, *17*, 7079–7085. [[CrossRef](#)]
74. Chai, G.; Dong, G.; Qiu, J.; Zhang, Q.; Yang, Z. 2.7  $\mu\text{m}$  Emission from Transparent  $\text{Er}^{3+}$ ,  $\text{Tm}^{3+}$  Codoped Yttrium Aluminum Garnet ( $\text{Y}_3\text{Al}_5\text{O}_{12}$ ) Nanocrystals–Tellurate Glass Composites by Novel Comelting Technology. *J. Phys. Chem. C* **2012**, *116*, 19941–19950. [[CrossRef](#)]
75. Nakanishi, T.; Katayama, Y.; Ueda, J.; Honma, T.; Tanabe, S.; Komatsu, T. Fabrication of Eu:  $\text{SrAl}_2\text{O}_4$ -based glass ceramics using Frozen sorbet method. *J. Ceram. Soc. Jpn.* **2011**, *119*, 609–615. [[CrossRef](#)]
76. Nakanishi, T.; Tanabe, S. Novel  $\text{Eu}^{2+}$ -Activated Glass Ceramics Precipitated with Green and Red Phosphors for High-Power White LED. *IEEE J. Sel. Top. Quantum Electron.* **2009**, *15*, 1171–1176. [[CrossRef](#)]
77. Nakanishi, T.; Tanabe, S. Preparation and luminescent properties of  $\text{Eu}^{2+}$ -activated glass ceramic phosphor precipitated with  $\beta\text{-Ca}_2\text{SiO}_4$  and  $\text{Ca}_3\text{Si}_2\text{O}_7$ . *Phys. Status Solidi A* **2009**, *206*, 919–922. [[CrossRef](#)]
78. Hench, L.L.; West, J.K. The Sol-Gel Process. *Chem. Rev.* **1990**, *90*, 33–72. [[CrossRef](#)]
79. Ciriminna, R.; Fidalgo, A.; Pandarus, V.; Beland, F.; Ilharco, L.M.; Pagliaro, M. The sol-gel route to advanced silica-based materials and recent applications. *Chem. Rev.* **2013**, *113*, 6592–6620. [[CrossRef](#)]
80. Gorni, G.; Velázquez, J.J.; Mosa, J.; Balda, R.; Fernández, J.; Durán, A.; Castro, Y. Transparent Glass-Ceramics Produced by Sol-Gel: A Suitable Alternative for Photonic Materials. *Materials* **2018**, *11*, 212. [[CrossRef](#)] [[PubMed](#)]
81. Bocker, C.; Bhattacharyya, S.; Höche, T.; Rüssel, C. Size distribution of  $\text{BaF}_2$  nanocrystallites in transparent glass ceramics. *Acta Mater.* **2009**, *57*, 5956–5963. [[CrossRef](#)]
82. Kajihara, K. Recent advances in sol-gel synthesis of monolithic silica and silica-based glasses. *J. Asian Ceram. Soc.* **2018**, *1*, 121–133. [[CrossRef](#)]
83. Prakashan, V.P.; Sajna, M.S.; Gejo, G.; Sanu, M.S.; Biju, P.R.; Cyriac, J.; Unnikrishnan, N.V. Perceiving impressive optical properties of ternary  $\text{SiO}_2\text{-TiO}_2\text{-ZrO}_2\text{:Eu}^{3+}$  sol-gel glasses with high reluctance for concentration quenching: An experimental approach. *J. Non-Cryst. Solids* **2018**, *482*, 116–125. [[CrossRef](#)]
84. Liu, X.; Jin, Z.; Bu, S.; Yin, T. Influences of Solvent on Properties of  $\text{TiO}_2$  Porous Films Prepared by a Sol-Gel Method from the System Containing PEG. *J. Sol-Gel Sci. Technol.* **2005**, *36*, 103–111. [[CrossRef](#)]
85. Zhou, L.; Chen, D.; Luo, W.; Wang, Y.; Yu, Y.; Liu, F. Transparent glass ceramic containing  $\text{Er}^{3+}$ :  $\text{CaF}_2$  nano-crystals prepared by sol-gel method. *Mater. Lett.* **2007**, *61*, 3988–3990. [[CrossRef](#)]
86. Jun, S.; Lee, J.; Jang, E. Highly Luminescent and Photostable Quantum Dot-Silica Monolith and Its Application to Light-Emitting Diodes. *ACS NANO* **2013**, *7*, 1472–1477. [[CrossRef](#)]
87. Cui, H.; Wang, M.; Ren, W.; Liu, Y.; Zhao, Y. Highly transparent silica monoliths embedded with high concentration oxide nanoparticles. *J. Sol-Gel Sci. Technol.* **2013**, *66*, 512–517. [[CrossRef](#)]
88. Stato, R.; Benino, Y.; Fujiwara, T.; Komatsu, T. YAG laser-induced crystalline dot patterning in samarium tellurite glasses. *J. Non-Cryst. Solids* **2001**, *289*, 228–232. [[CrossRef](#)]
89. Honma, T.; Benino, Y.; Fujiwara, T.; Komatsu, T.; Sato, R. Nonlinear optical crystal-line writing in glass by yttrium aluminum garnet laser irradiation. *Appl. Phys. Lett.* **2003**, *82*, 892–894. [[CrossRef](#)]
90. Hasegawa, S.; Shinozaki, K.; Honma, T.; Dimitrov, V.; Kim, H.G.; Komatsu, T. Dielectric properties of glass-ceramics with  $\text{Ba}_{1-x}\text{Y}_{2x/3}\text{Nb}_2\text{O}_6$  nanocrystals and laser patterning of highly oriented crystal lines. *J. Non-Cryst. Solids* **2016**, *452*, 74–81. [[CrossRef](#)]

91. Abe, M.; Benino, Y.; Fujiwara, T.; Komatsu, T.; Sato, R. Writing of nonlinear optical  $\text{Sm}_2(\text{MoO}_4)_3$  crystal lines at the surface of glass by samarium atom heat processing. *J. Appl. Phys.* **2005**, *97*, 123516. [CrossRef]
92. Miura, K.; Qiu, J.; Inouye, H.; Mitsuyu, T.; Hirao, K. Photowritten optical waveguides in various glasses with ultrashort pulse laser. *Appl. Phys. Lett.* **1997**, *71*, 3329–3331. [CrossRef]
93. Honma, T.; Benino, Y.; Fujiwara, T.; Komatsu, T. Line patterning with large refractive index changes in the deep inside of glass by nanosecond pulsed YAG laser irradiation. *Solid State Commun.* **2005**, *135*, 193–196. [CrossRef]
94. Petrov, A.Y. A new dimension for nonlinear photonic crystals. *Nat. Photonics* **2018**, *12*, 570–571. [CrossRef]
95. Liu, S.; Switkowski, K.; Xu, C.; Tian, J.; Wang, B.; Lu, P.; Krolikowski, W.; Sheng, Y. Nonlinear wavefront shaping with optically induced three-dimensional nonlinear photonic crystals. *Nat. Commun.* **2019**, *10*, 3208. [CrossRef]
96. Wei, D.; Wang, C.; Wang, H.; Hu, X.; Wei, D.; Fang, X.; Zhang, Y.; Wu, D.; Hu, Y.; Li, J.; et al. Experimental demonstration of a three-dimensional lithium niobate nonlinear photonic crystal. *Nat. Photonics* **2018**, *12*, 596–600. [CrossRef]
97. Xu, T.; Switkowski, K.; Chen, X.; Liu, S.; Koynov, K.; Yu, H.; Zhang, H.; Wang, J.; Sheng, Y.; Krolikowski, W. Three-dimensional nonlinear photonic crystal in ferroelectric barium calcium titanate. *Nat. Photonics* **2018**, *12*, 591–595. [CrossRef]
98. Chen, F.; De Aldana, J.R.V. Optical waveguides in crystalline dielectric materials produced by femtosecond-laser micromachining. *Laser Photonics Rev.* **2014**, *8*, 251–275. [CrossRef]
99. Stone, A.; Sakakura, M.; Shimotsuna, Y.; Miura, K.; Hirao, K.; Dierolf, V.; Jain, H. Femtosecond laser-writing of 3D crystal architecture in glass: Growth dynamics and morphological control. *Mater. Des.* **2018**, *146*, 228–238. [CrossRef]
100. Huang, X.; Guo, Q.; Yang, D.; Xiao, X.; Liu, X.; Xia, Z.; Fan, F.; Qiu, J.; Dong, G. Reversible 3D laser printing of perovskite quantum dots inside a transparent medium. *Nat. Photonics* **2019**, *14*, 82–88. [CrossRef]
101. Xia, M.; Luo, J.; Chen, C.; Liu, H.; Tang, J. Semiconductor Quantum Dots-Embedded Inorganic Glasses: Fabrication, Luminescent Properties, and Potential Applications. *Adv. Opt. Mater.* **2019**, *7*, 1900851. [CrossRef]
102. Miura, K.; Qiu, J.; Mitsuyu, T. Space-selective growth of frequency-conversion crystals in glasses with ultrashort infrared laser pulses. *Opt. Lett.* **2000**, *25*, 408–410. [CrossRef]
103. Peruchon, L.; Puzenat, E.; Herrmann, J.M.; Guillard, C. Photocatalytic efficiencies of self-cleaning glasses. Influence of physical factors. *Photochem. Photobiol. Sci.* **2009**, *8*, 1040–1046. [CrossRef]
104. Ponraj, C.; Vinitha, G.; Daniel, J. A review on the visible light active  $\text{BiFeO}_3$  nanostructures as suitable photocatalyst in the degradation of different textile dyes. *Environ. Nanotechnol. Monit. Manag.* **2017**, *7*, 110–120.
105. Soltani, T.; Lee, B.-K. Enhanced formation of sulfate radicals by metal-doped  $\text{BiFeO}_3$  under visible light for improving photo-Fenton catalytic degradation of 2-chlorophenol. *Chem. Eng. J.* **2017**, *313*, 1258–1268. [CrossRef]
106. Soltani, T.; Lee, B.-K. Improving heterogeneous photo-Fenton catalytic degradation of toluene under visible light irradiation through Ba-doping in  $\text{BiFeO}_3$  nanoparticles. *J. Mol. Catal. A Chem.* **2016**, *425*, 199–207. [CrossRef]
107. Masai, H.; Fujiwara, T.; Mori, H. Effect of  $\text{SnO}$  addition on optical absorption of bismuth borate glass and photocatalytic property of the crystallized glass. *Appl. Phys. Lett.* **2008**, *92*, 141902. [CrossRef]
108. Masai, H.; Toda, T.; Takahashi, Y.; Fujiwara, T. Fabrication of anatase precipitated glass-ceramics possessing high transparency. *Appl. Phys. Lett.* **2009**, *94*, 151910. [CrossRef]
109. Yoshida, K.; Takahashi, Y.; Ihara, R.; Terakado, N.; Fujiwara, T.; Kato, H.; Kakihana, M. Large enhancement of photocatalytic activity by chemical etching of  $\text{TiO}_2$  crystallized glass. *APL Mater.* **2014**, *2*, 106103. [CrossRef]
110. Kumar, S.; Kushwaha, H.S.; Singh, V.P.; Vaish, R.; Ilahi, B.; Madhar, N.A. Solar light induced antibacterial performance of  $\text{TiO}_2$  crystallized glass ceramics. *Int. J. Appl. Glass Sci.* **2018**, *9*, 480–486. [CrossRef]
111. Ida, T.; Shinozaki, K.; Honma, T.; Komatsu, T. Synthesis and photocatalytic properties of  $\alpha\text{-ZnWO}_4$  nanocrystals in tungsten zinc borate glasses. *J. Asian Ceram. Soc.* **2018**, *2*, 253–257. [CrossRef]
112. Sharma, S.K.; Singh, V.P.; Chauhan, V.S.; Kushwaha, H.S.; Vaish, R. Photocatalytic Active Bismuth Fluoride/Oxyfluoride Surface Crystallized  $2\text{Bi}_2\text{O}_3\text{-B}_2\text{O}_3$  Glass-Ceramics. *J. Electron. Mater.* **2018**, *47*, 3490–3496. [CrossRef]
113. Sharma, S.K.; Singh, V.P.; Bhargava, A.; Park, S.-H.; Chauhan, V.S.; Vaish, R. Surface crystallization of  $\text{BiOCl}$  on  $2\text{Bi}_2\text{O}_3\text{-B}_2\text{O}_3$  glasses for photocatalytic applications. *J. Mater. Sci. Mater. Electron.* **2021**, *32*, 10520–10531. [CrossRef]
114. Singh, V.P.; Vaish, R. Controlled crystallization of photocatalytic active Bismuth oxyfluoride/Bismuth fluoride on  $\text{SrO-Bi}_2\text{O}_3\text{-B}_2\text{O}_3$  transparent glass ceramic. *J. Eur. Ceram. Soc.* **2018**, *38*, 3635–3642. [CrossRef]
115. Singh, V.P.; Vaish, R. Hierarchical growth of  $\text{BiOCl}$  on  $\text{SrO-Bi}_2\text{O}_3\text{-B}_2\text{O}_3$  glass-ceramics for self-cleaning applications. *J. Am. Ceram. Soc.* **2018**, *101*, 2901–2913. [CrossRef]
116. Singh, G.; Singh, V.; Vaish, R. Controlled crystallization of  $\text{BiOCl/BiF}_3$  on  $\text{ZnO-Bi}_2\text{O}_3\text{-B}_2\text{O}_3$  glass surfaces for photocatalytic and self-cleaning applications. *Materialias* **2019**, *5*, 100196. [CrossRef]
117. Thakur, V.; Kushwaha, H.S.; Singh, A.; Vaish, R.; Punia, R.; Singh, L. A study on the structural and photocatalytic degradation of ciprofloxacin using  $(70\text{Bi}_2\text{O}_3\text{-}29\text{Bi}_2\text{O}_3\text{-}1\text{Dy}_2\text{O}_3)\text{-}x(\text{BaO-TiO}_2)$  glass ceramics. *J. Non-Cryst. Solids* **2015**, *428*, 197–203. [CrossRef]
118. Kushwaha, H.S.; Thomas, P.; Vaish, R. Visible light driven multifunctional photocatalysis in  $\text{TeO}_2$ -based semiconductor glass ceramics. *J. Photonics Energy* **2017**, *7*, 016502. [CrossRef]
119. Iida, Y.; Akiyama, K.; Kobzi, B.; Sinkó, K.; Homonnay, Z.; Kuzmann, E.; Ristić, M.; Krehula, S.; Nishida, T.; Kubuki, S. Structural analysis and visible light-activated photocatalytic activity of iron-containing soda lime aluminosilicate glass. *J. Alloys Compd.* **2015**, *645*, 1–6. [CrossRef]

120. Margha, F.H.; Radwan, E.K.; Badawy, M.I.; Gad-Allah, T.A. Bi<sub>2</sub>O<sub>3</sub>-BiFeO<sub>3</sub> Glass-Ceramic: Controllable β-/γ-Bi<sub>2</sub>O<sub>3</sub> Transformation and Application as Magnetic Solar-Driven Photocatalyst for Water Decontamination. *ACS Omega* **2020**, *5*, 14625–14634. [[CrossRef](#)] [[PubMed](#)]
121. Kadam, S.R.; Panmand, R.P.; Sonawane, R.S.; Gosavi, S.W.; Kale, B.B. A stable Bi<sub>2</sub>S<sub>3</sub> quantum dot-glass nanosystem: Size tuneable photocatalytic hydrogen production under solar light. *RSC Adv.* **2015**, *5*, 58485–58490. [[CrossRef](#)]
122. Li, G.; Huang, S.; Shen, Y.; Lou, Z.; Yuan, H.; Zhu, N.; Wei, Y. Synthesis of an efficient lanthanide doped glass-ceramic based near-infrared photocatalyst by a completely waterless solid-state reaction method. *Dalton Trans.* **2019**, *48*, 9925–9929. [[CrossRef](#)]
123. Li, G.; Huang, S.; Yuan, H.; Zhu, N.; Wei, Y. Efficient and regenerative near-infrared glass-ceramic photocatalyst fabricated by a facile in-situ etching method. *Chem. Eng. J.* **2020**, *394*, 124877. [[CrossRef](#)]
124. Li, G.; Huang, S.; Zhu, N.; Yuan, H.; Ge, D.; Wei, Y. Defect-rich heterojunction photocatalyst originated from the removal of chloride ions and its degradation mechanism of norfloxacin. *Chem. Eng. J.* **2021**, *421*, 127852. [[CrossRef](#)]
125. Li, G.; Huang, S.; Zhu, N.; Yuan, H.; Ge, D. Near-infrared responsive upconversion glass-ceramic@BiOBr heterojunction for enhanced photodegradation performances of norfloxacin. *J. Hazard. Mater.* **2021**, *403*, 123981. [[CrossRef](#)]
126. Zhihan, Z.; Bofeng, Z.; Dong, W.; Qi, Z.; Cong, T.; Nanwen, Z.; Guobiao, L. A Yb<sup>3+</sup>/Er<sup>3+</sup> co-doped Bi<sub>1.95</sub>Yb<sub>0.04</sub>Er<sub>0.01</sub>V<sub>2</sub>O<sub>8</sub> efficient upconversion glass-ceramic photocatalyst for antibiotic degradation driven by UV-Vis-NIR broad spectrum light. *Appl. Surf. Sci.* **2022**, *583*, 152565. [[CrossRef](#)]
127. Li, G.; Huang, S.; Li, K.; Zhu, N.; Zhao, B.; Zhong, Q.; Zhang, Z.; Ge, D.; Wang, D. Near-infrared responsive Z-scheme heterojunction with strong stability and ultra-high quantum efficiency constructed by lanthanide-doped glass. *Appl. Catal. B Environ.* **2022**, *311*, 121363. [[CrossRef](#)]
128. Shaikh, S.; Kedia, S.; Singh, A.K.; Sharma, K.; Sinha, S. Surface treatment of 45S5 Bioglass using femtosecond laser to achieve superior growth of hydroxyapatite. *J. Laser Appl.* **2017**, *29*, 022004. [[CrossRef](#)]
129. Amanov, A.; Pyun, Y.S.; Vasudevan, V.K. High Strength and Wear Resistance of Tantalum by Ultrasonic Nanocrystalline Surface Modification Technique at High Temperatures. *IOP Conf. Ser. Mater. Sci. Eng.* **2017**, *194*, 012032. [[CrossRef](#)]
130. Fu, H.; Zhang, S.; Xu, T.; Zhu, Y.; Chen, J. Photocatalytic Degradation of RhB by Fluorinated Bi<sub>2</sub>WO<sub>6</sub> and Distributions of the Intermediate Products. *Environ. Sci. Technol.* **2008**, *42*, 2085–2091. [[CrossRef](#)]
131. Jiang, H.-Y.; Liu, J.; Cheng, K.; Sun, W.; Lin, J. Enhanced Visible Light Photocatalysis of Bi<sub>2</sub>O<sub>3</sub> upon Fluorination. *J. Phys. Chem. C* **2013**, *117*, 20029–20036. [[CrossRef](#)]
132. Liu, S.; Yin, K.; Ren, W.; Cheng, B.; Yu, J. Tandem photocatalytic oxidation of Rhodamine B over surface fluorinated bismuth vanadate crystals. *J. Mater. Chem.* **2012**, *22*, 17759–17767. [[CrossRef](#)]
133. Liu, S.; Yu, J.; Cheng, B.; Jaroniec, M. Fluorinated semiconductor photocatalysts: Tunable synthesis and unique properties. *Adv Colloid Interface Sci.* **2012**, *173*, 35–53. [[CrossRef](#)]
134. Berthier, T.; Fokin, V.M.; Zanotto, E.D. New large grain, highly crystalline, transparent glass-ceramics. *J. Non-Cryst. Solids* **2008**, *354*, 1721–1730. [[CrossRef](#)]
135. Baia, L.; Stefan, R.; Kiefer, W.; Popp, J.; Simon, S. Structural investigations of copper doped B<sub>2</sub>O<sub>3</sub>-Bi<sub>2</sub>O<sub>3</sub> glasses with high bismuth oxide content. *J. Non-Cryst. Solids* **2001**, *303*, 379–386.
136. Cao, S.; Guo, C.; Lv, Y.; Guo, Y.; Liu, Q. A novel BiOCl film with flowerlike hierarchical structures and its optical properties. *Nanotechnol.* **2009**, *20*, 275702. [[CrossRef](#)] [[PubMed](#)]
137. Al-Baradi, A.M.; Wahab, E.a.A.; Shaaban, K.S. Preparation and Characteristics of B<sub>2</sub>O<sub>3</sub>-SiO<sub>2</sub>-Bi<sub>2</sub>O<sub>3</sub>-TiO<sub>2</sub>-Y<sub>2</sub>O<sub>3</sub> Glasses and Glass-Ceramics. *Silicon* **2021**, *14*, 5277–5287. [[CrossRef](#)]
138. Milewska, K.; Maciejewski, M.; Synak, A.; Lapinski, M.; Mielewczyk-Gryn, A.; Sadowski, W.; Koscielska, B. From Structure to Luminescent Properties of B<sub>2</sub>O<sub>3</sub>-Bi<sub>2</sub>O<sub>3</sub>-SrF<sub>2</sub> Glass and Glass-Ceramics Doped with Eu<sup>3+</sup> Ions. *Materials* **2021**, *14*, 4490. [[CrossRef](#)]
139. Jamalalah, B.C.; Viswanadha, G. Erbium doped Bi<sub>2</sub>O<sub>3</sub>-B<sub>2</sub>O<sub>3</sub> glass-ceramics containing Bi<sub>3</sub>B<sub>5</sub>O<sub>12</sub> and CaF<sub>2</sub> nanocrystallites for 1.53 μm fiber lasers. *J. Eur. Ceram. Soc.* **2020**, *40*, 4578–4588. [[CrossRef](#)]
140. Li, M.; Zhou, X.; Zhang, Y.; Jiang, F.; Sha, S.; Xu, S.; Li, S. Preparation and upconversion luminescent properties of Yb<sup>3+</sup>/Er<sup>3+</sup> doped transparent glass-ceramics containing CaF<sub>2</sub> nanocrystals. *Ceram. Int.* **2020**, *46*, 25399–25404. [[CrossRef](#)]
141. Panyata, S.; Eitsayeam, S.; Tunkasiri, T.; Munpakdee, A.; Pengpat, K. Crystallization kinetic of Er<sup>3+</sup>-doped BiO<sub>1.5</sub>-GeO<sub>2</sub>-BO<sub>1.5</sub> glass-ceramic. *Ceram. Int.* **2018**, *44*, S46–S49. [[CrossRef](#)]
142. Sahu, S.P.; Cates, S.L.; Kim, H.I.; Kim, J.H.; Cates, E.L. The Myth of Visible Light Photocatalysis Using Lanthanide Upconversion Materials. *Environ. Sci Technol.* **2018**, *52*, 2973–2980. [[CrossRef](#)]
143. Takata, T.; Jiang, J.; Sakata, Y.; Nakabayashi, M.; Shibata, N.; Nandal, V.; Seki, K.; Hisatomi, T.; Domen, K. Photocatalytic water splitting with a quantum efficiency of almost unity. *Nature* **2020**, *581*, 411–414. [[CrossRef](#)]
144. Djurišić, A.B.; He, Y.; Ng, A.M.C. Visible-light photocatalysts: Prospects and challenges. *APL Mater.* **2020**, *8*, 030903. [[CrossRef](#)]